Stem Cell Reports
Article

ISSCR

OPEN ACCESS

Homozygous ALS-linked *FUS* P525L mutations cell- autonomously perturb transcriptome profile and chemoreceptor signaling in human iPSC microglia

Sze Yen Kerk,[1,*] Yu Bai,[1] Janell Smith,[1] Pranav Lalgudi,[1] Charleen Hunt,[1] Junko Kuno,[1] John Nuara,[1] Tao Yang,[1] Kathryn Lanza,[1] Newton Chan,[1] Angel Coppola,[1] Qian Tang,[1] Jennifer Espert,[1] Henderson Jones,[1] Casey Fannell,[1] Brian Zambrowicz,[1] and Eric Chiao[1,*]

[1]Regeneron Pharmaceuticals, Tarrytown, NY 10591, USA

*Correspondence: eric.chiao@regeneron.com (E.C.), john.kerk@regeneron.com (S.Y.K.)

https://doi.org/10.1016/j.stemcr.2022.01.004

SUMMARY

Amyotrophic lateral sclerosis is a fatal disease pathologically typified by motor and cortical neurodegeneration as well as microgliosis. The *FUS* P525L mutation is highly penetrant and causes ALS cases with earlier disease onset and more aggressive progression. To date, how P525L mutations may affect microglia during ALS pathogenesis had not been explored. In this study, we engineered isogenic control and P525L mutant *FUS* in independent human iPSC lines and differentiated them into microglia-like cells. We report that the P525L mutation causes FUS protein to mislocalize from the nucleus to cytoplasm. Homozygous P525L mutations perturb the transcriptome profile in which many differentially expressed genes are associated with microglial functions. Specifically, the dysregulation of several chemoreceptor genes leads to altered chemoreceptor-activated calcium signaling. However, other microglial functions such as phagocytosis and cytokine release are not significantly affected. Our study underscores the cell-autonomous effects of the ALS-linked *FUS* P525L mutation in a human microglia model.

INTRODUCTION

Amyotrophic lateral sclerosis (ALS) is a fatal, progressive motor neurodegenerative disease for which no cure yet exists. A thorough understanding of its pathogenesis is hampered by the sporadic and idiopathic nature of the majority of disease instances. However, ~10% of ALS cases are familial and genetically linked. To date, mutations in >50 genes have been associated with familial and sporadic ALS, although the mechanisms by which they contribute to disease are poorly understood. Roughly two-thirds of familial occurrences can be attributed to mutations located in 4 genes: *C9ORF72*, *TARDBP*, *SOD1*, and *FUS* (Taylor et al., 2016). ALS-linked *FUS* mutations are highly penetrant and associated with earlier disease onset and more aggressive progression (Ji et al., 2017; Souza et al., 2015). The discovery that FUS protein mislocalization occurs in motor neurons of sporadic ALS patients also highlights its potential role in the majority of ALS cases (Tyzack et al., 2019). Despite extensive research, the exact cell types underlying ALS etiology are still unclear even for disease instances driven by familial mutations (Hickman et al., 2018).

FUS is a ubiquitously expressed gene. In the human adult central nervous system (CNS), it seems to be more highly transcribed in microglia compared to neurons and other glial cells (Zhang et al., 2016). The FUS protein is predominantly nuclear due to its nuclear localization signal (NLS) and can undergo liquid-liquid phase separation owing to its prion-like domains (Portz et al., 2021). FUS also possesses RNA- and DNA-binding domains and has been functionally implicated in DNA repair and RNA processing such as transcription, splicing, transport, and translation. More than 50 mutations in *FUS* have been identified in families afflicted with ALS. The majority are dominant missense mutations largely clustered within the NLS or prion-like domains of the protein. One such mutation found in the NLS, P525L, causes juvenile-onset forms of ALS that are highly aggressive and penetrant (Kuang et al., 2017; Shang and Huang, 2016).

Pathologically, ALS is typified not just by motor and cortical neurodegeneration but also by microgliosis, where microglia become activated, change their morphology, gene expression, and exhibit altered motility, phagocytosis, and cytokine release functions (Clarke and Patani, 2020; Li and Barres, 2018). To date, how *FUS* P525L mutations may affect microglia during ALS pathogenesis had not been explored. To bridge this knowledge gap, we postulated that microglia derived from human induced pluripotent stem cells (iPSC) harboring *FUS* P525L would display transcriptional and functional changes. To test this hypothesis, we generated isogenic control and P525L mutant *FUS* using CRISPR (clustered regularly interspaced short palindromic repeats) technology in 2 independent human iPSC lines. The engineered cell lines possessing the series of *FUS* genotypes were then differentiated into microglia-like cells (MIGs). Immunocytochemistry demonstrated that the P525L mutation caused FUS protein to be mislocalized from the nucleus to the cytoplasm. RNA sequencing (RNA-seq) and intracellular calcium flux assays revealed that homozygous *FUS* P525L mutations perturbed the transcriptome profile and specific chemoreceptor signaling of

MIGs. However, other microglial functions such as phagocytosis and cytokine release were not significantly altered when examined by a panel of *in vitro* assays. Our study underscores the cell-autonomous effects of the ALS-linked *FUS* P525L mutation in a human microglia model.

RESULTS

CRISPR engineering of *FUS* P525L mutations and isogenic controls in independent human iPSC lines

Considering its penetrant and aggressive pathogenicity in ALS, we focused on the *FUS* P525L point mutation (Naumann et al., 2019), located in the NLS region (Figure 1A), to study its effects on human iPSC-derived MIGs. Due to our lack of access to P525L patient samples, we engineered a *FUS* genotypic series of P525L mutations in 2 independent wild-type (WT) human iPSC lines, AG (Figure 1B) and JK (Figure S1A), to minimize any line-specific phenotypic differences due to their unique genetic backgrounds. The parental WT iPSC lines were derived by reprogramming 2 independent fibroblast lines using non-genome-integrating factors. Via CRISPR technology, *FUS* P525L homozygotes (Hom) were generated from WT iPSC lines using a single guide RNA (sgRNA), in which the middle nucleotide of the protospacer-adjacent motif (PAM) shared the same position as the desired point mutation. This obviated the need to introduce silent mutations within the single-stranded oligodeoxynucleotide (ssODN) repair template to prevent Cas9 re-cutting upon successful targeting. To generate P525L heterozygotes (Het), equimolar amounts of the mutant ssODN and a control ssODN containing 2 synonymous point mutations to prevent Cas9 re-cutting were used. By using this strategy, engineered controls (eCtrl) that were repaired biallelically with control ssODN were also obtained and treated as putative WT equivalents. Quality controls were performed via array comparative genomic hybridization (aCGH) to ensure no gross karyotypic abnormalities and single-nucleotide polymorphism (SNP) microarrays to exclude clones with copy-neutral loss-of-heterozygosity (CN-LOH) affecting entire chromosome arms (Figure S1C) (Weisheit et al., 2020). In summary, 2 independent, karyotypically normal, isogenic iPSC series of *FUS* genotypes encompassing WT, eCtrl, P525L Het, and P525L Hom were successfully engineered.

We also generated a *FUS* knockout (KO) clone in the iPSC AG line by biallelically deleting the entire *FUS* coding sequence using flanking sgRNAs (Figure 1B). Immunocytochemistry with an antibody against the FUS protein showed largely nuclear signals in both WT and eCtrl clones as expected and no detectable signal in the KO, confirming the successful deletion of *FUS* as well as the specificity of the anti-FUS antibody. Of particular note is the characteristic FUS exclusion from nucleolar regions in the nucleus as previously reported (Yang et al., 2015). In P525L Hom, FUS was predominantly seen in the cytoplasm due to both chromosomal copies having mutated NLS, whereas in P525L Het cells, FUS was observed in both the nucleus and cytoplasm, likely representing the WT and mutant forms, respectively (Figures 1C and S1B). These observations of FUS subcellular localizations further confirmed the various genotypes of engineered iPSC lines and are consistent with published FUS immunostaining results in human fibroblasts from P5252L mutation carriers (Lo Bello et al., 2017).

Directed differentiation of human iPSC lines with *FUS* P525L mutations and isogenic controls into MIGs

To study the effects of *FUS* P525L mutation in human microglia, we adopted the established protocol from Douvaras et al. (2017) to sequentially direct the differentiation of our CRISPR-engineered iPSC lines through an initial mesodermal lineage, followed by an intermediate myeloid progenitor stage, and finally into MIGs (Figure 2A). This strategy attempted to recapitulate the differentiation process of microglia during embryonic development, which was elucidated a decade prior (Ginhoux et al., 2013). In our pilot experiment, iPSC AG lines with the following genotypes were differentiated: *FUS* WT, eCtrl, P525L Het (2 clones), P525L Hom (2 clones), and KO. The experimental design encompassed 4 differentiation replicates per iPSC clone and myeloid progenitor harvests at 4 different time points. At the intermediate stage, adherent precursor cells continually generated free-floating myeloid progenitors marked by the membrane protein CD14 (Figures S2A and S2B), which were then periodically harvested, plated, and further differentiated into MIGs by applying interleukin (IL)-34, the CSF1R ligand in the brain that is crucial for microglia development (Wang et al., 2012). This pilot aimed to validate the molecular identity of the differentiated MIGs and determine its reproducibility across different harvest time points.

Immunosurveillance is one of the characteristic functions of microglia whose ramified processes continuously surveil the extracellular microenvironment for foreign or unwanted matter, which is then internalized via phagocytosis (Prinz et al., 2019). The iPSC lines of the *FUS* genotypic series gave rise to MIGs with motile pseudopodia and putative phagosomes migrating from cell edge to soma (Figure 2B; Videos S1A and S1B). These cells expressed microglial markers such as P2RY12, CX3CR1, MERTK, MRC1, and TREM2 at percentages that were well within reported ranges (Figures 2C and 2D) (Douvaras et al., 2017). Many of these marker proteins have well-established microglial functions such as target recognition, chemotaxis, and apoptosis (Prinz et al., 2019). Also confirmed was the expression of MEF2C, a transcription factor hypothesized

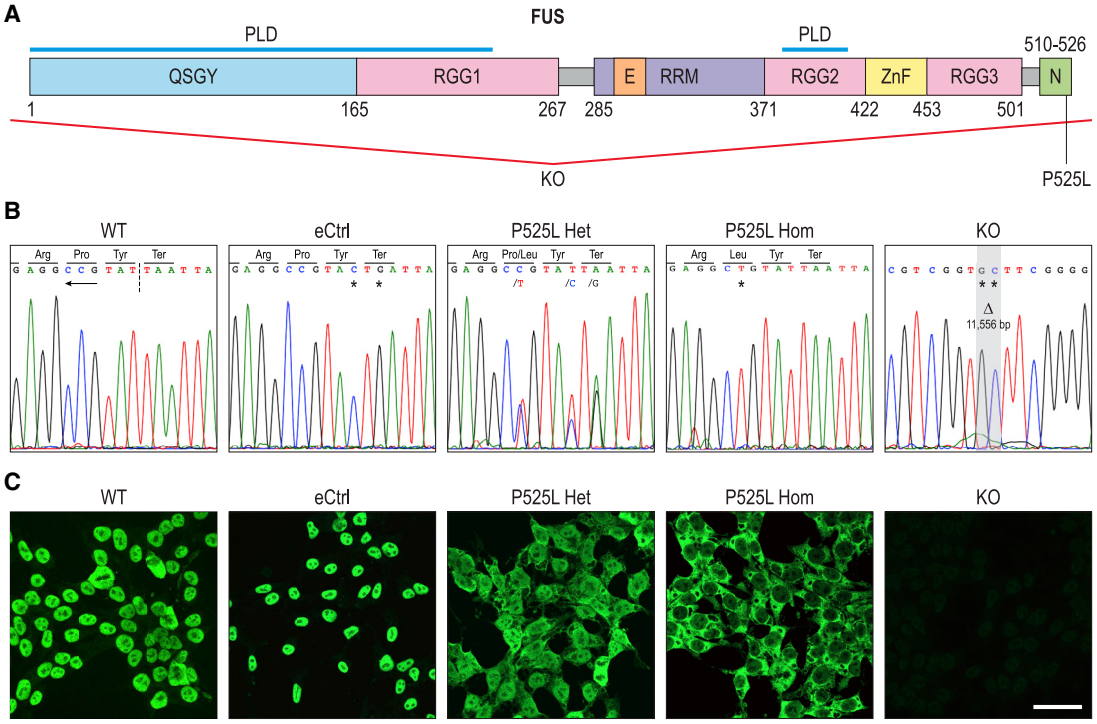

Figure 1. CRISPR engineering of *FUS* P525L mutations and isogenic controls in independent human iPSC lines

(A) Schematic of human FUS protein and its domains. QSGY and RGG, regions rich in the stated amino acids; PLD, prion-like domain; E, nuclear export signal; RRM, RNA recognition motif; ZnF, zinc finger domain; N, NLS. Numbers indicate amino acid positions. Red lines denote deletion of the entire *FUS* coding sequence in the KO.

(B) Sanger sequencing of CRISPR-engineered *FUS* genomic locus in human iPSC lines. In the WT panel, the inverted NGG PAM site is underlined by the arrow, whereas the Cas9 endonuclease cut site is bisected by the perforated line. Homozygous point mutations compared to WT, such as that in P525L Hom, are denoted by asterisks. Heterozygous point mutations such as those in P525L Het are denoted by a slash, followed by the mutant allele. In the KO, the gray area represents a homozygous deletion (Δ) of 11,556 bp containing the entire *FUS* coding sequence, substituted by 2 point mutations.

(C) Immunocytochemistry of FUS protein revealing its subcellular localization in iPSCs of different genotypes. To better visualize the cytoplasmic compartment, iPSCs were dissociated into single cells and plated with ROCK inhibitor Y-27632, which causes cells to stretch out on the culture surface. Apparent variations in cell size are due to fixations being performed at different stages of cell-plate adherence. Scale bar, 50 μm. Presented here are clones from the AG line; see Figure S1 for the JK line.

to specify microglial identity (Lavin et al., 2014), as well as TBK1 and MAP3K7 (Figure S2C). A heterozygous *Tbk1* mouse model with *Map3k7* heterozygosity spatially induced in myeloid cells displayed ALS-like neurodegeneration phenotypes (Xu et al., 2018). In addition, FUS subcellular localizations in MIGs across the different genotypes mirrored those observed in corresponding iPSCs as expected (Figures 1C and 2D).

Identity validation via RNA-seq of iPSC-derived MIGs with *FUS* P525L mutations and isogenic controls

In the pilot transcriptome profiling experiment, the MIGs of the *FUS* genotypic series and their preceding myeloid progenitors were subjected to next-generation RNA-seq. Principal component analysis (PCA) of transcriptome profiles showed that MIGs were differentiated from their progenitors as these 2 groups clustered distinctly from each other (Figures 3A and 3B). This analysis also revealed that cells of different *FUS* genotypes were very similar in transcriptome profiles and grouped closely together, although P525L Hom cells clustered slightly away from the other genotypes, hinting at significant transcriptional perturbations due to the homozygous mutation (Figure 3A). Moreover, PCA demonstrated that MIGs terminally differentiated from progenitor cells harvested from the first 3 time points between days 52 and 75 of differentiation were quite similar and clustered closely together, in contrast to those from day 115 (Figure 3B). As such, in subsequent differentiation and RNA-seq experiments, we would harvest cells from the earlier time points to be used as replicates.

We next compared the transcriptome profiles of our MIGs to those of purified human cortical microglia and

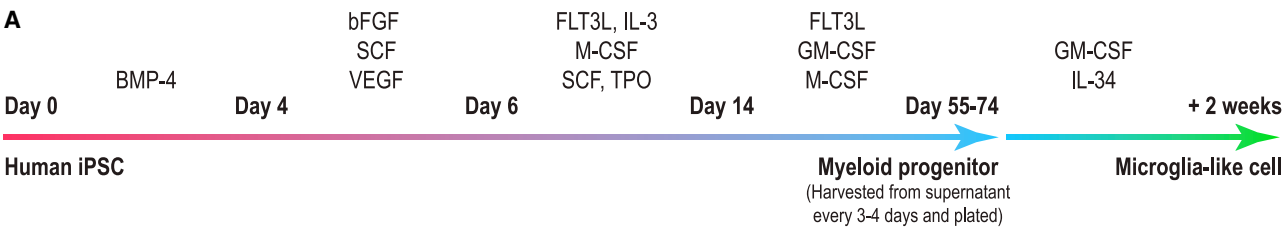

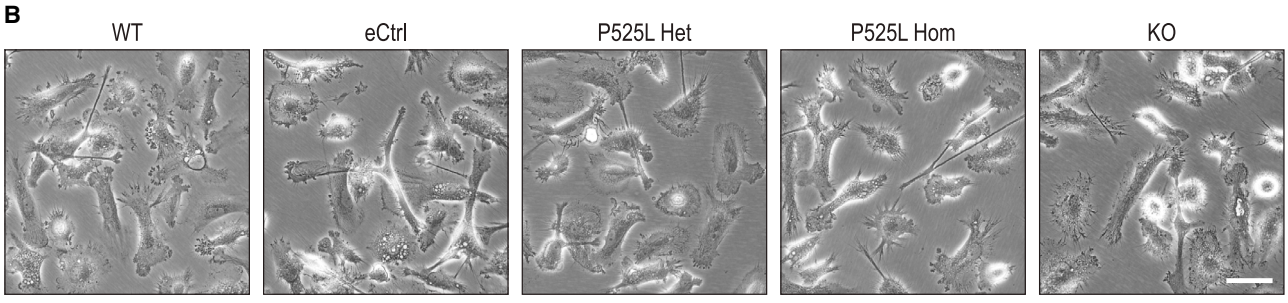

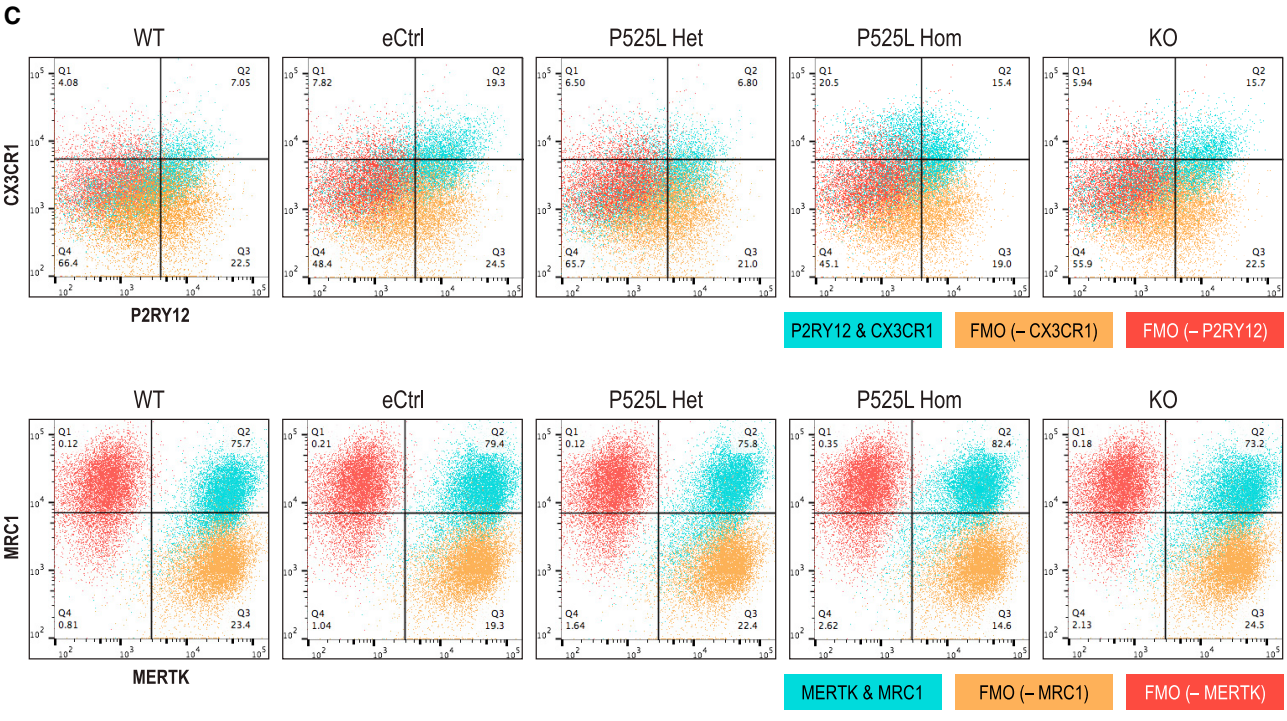

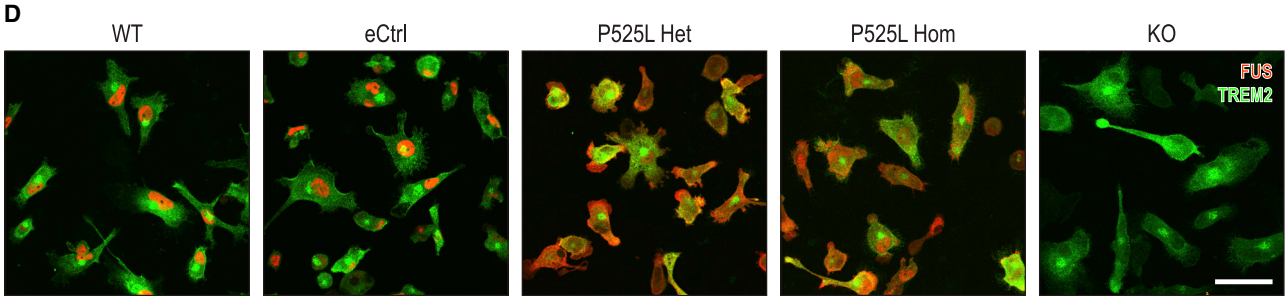

(legend on next page)

brain cortex as published by Galatro et al. (2017). The authors extracted RNA directly from isolated cells without an intervening *in vitro* culture step, which has been shown to alter the microglial transcriptome profile within 6 h (Gosselin et al., 2017). Qualitatively, the global gene expression patterns of the MIGs of various *FUS* genotypes were more similar to those of purified primary human microglia as opposed to brain cortex (Figure 3C). Quantitatively, this was corroborated by the higher Spearman's rank correlation coefficients calculated between the gene expression profiles of MIGs with primary microglia (0.7766 ± 0.0100) compared to those between MIGs with brain cortex (0.4799 ± 0.0050). The latter values were much closer to the coefficient calculated between primary microglia and cortex (0.4620) (Figure 3D). That the global gene expression pattern of our microglia-like cells was not identical to that of primary microglia indicates that there is room for optimization of this differentiation protocol; our results should thus be viewed with this caveat in mind.

At the individual gene level of our MIGs, we confirmed the expression of multiple microglial markers (Figures 3E and S3A), which have been well defined (Butovsky et al., 2014; Hickman et al., 2013) and widely referenced by other researchers to validate the identity of their iPSC-derived microglia (Abud et al., 2017; Douvaras et al., 2017; Muffat et al., 2016; Pandya et al., 2017). The mRNA levels of these genes were consistent across genotypes and the first 3 time points, while a lower trend was seen in cells from day 115, supporting our decision to exclude later time points from subsequent experiments (Figures 3E and S3A). It is worthy of note that the expression level of the microglial marker *TMEM119* was extremely low in our MIGs (Figure S3A) (Bennett et al., 2016), as was also observed by Abud et al. (2017) and Douvaras et al. (2017). The immunochemistry and transcriptome profiling results from our pilot experiment demonstrated the consistent generation of iPSC-derived MIGs across different *FUS* genotypes between days 52 and 75, whereas cells harvested beyond day 100 seemed to exhibit a downregulation of microglial markers.

Homozygous *FUS* P525L MIGs display transcriptional perturbations of genes associated with characteristic microglial functions

With the insights gained from our pilot studies, we proceeded to perform a larger-scale microglial differentiation experiment with both independent human iPSC lines, AG and JK, harboring the series of *FUS* WT, eCtrl, P525L Het, and P525L Hom genotypes. The experimental design encompassed 2 independent differentiation experiments whereby for each differentiation run, myeloid progenitors were harvested at 4 different time points between days 55 and 74 and terminally differentiated into MIGs as described above (Figure 4A). Following RNA-seq, PCA of the transcriptome profiles showed that MIGs across genotypes, replicates, and time points clustered together and were similar in identity (Figure 4B). A minor issue with the clonality of the JK WT line uncovered via RNA-seq is addressed in Figure S4B. In short, this line was contaminated with a small percentage of cells containing undesired CRISPR mutations in the *FUS* locus that fortuitously did not alter the FUS WT amino acid sequence. As such, data from this line were included in our analysis.

A closer look at *FUS* gene expression revealed that it was significantly increased in P525L Hom compared to WT and eCtrl; in P525L Het, the expression level was intermediate between that of Hom and controls (Figure 4C). Such an observation was expected since FUS binds to a highly conserved region around exon 7 and flanking introns of its own pre-mRNA and partially represses exon 7 splicing. This repression causes exon 7 skipping in a portion of transcripts where resultant variants undergo nonsense-mediated decay, which decreases overall *FUS* transcript levels. The ALS-causing mutations in FUS NLS, R521G and R522G, have been documented to disrupt this negative autoregulatory function, hence explaining the upregulation of *FUS* gene expression in MIGs with the P525L allele (Zhou et al., 2013).

To address the question of whether the *FUS* P525L mutation causes any transcriptional perturbations in human microglia, we compared the transcriptome profiles of MIGs of Het and Hom genotypes with those of WT and eCtrl. Differential gene expression levels were defined as significantly different by a transcript fold-change threshold of no less than 1.5 in either the up or down direction as well as a p value cutoff of <0.01. Comparisons were always performed individually in each independent line, AG and JK, before filtering for the overlap of the results. *FUS* eCtrl MIGs were compared to WT and only 6 differentially expressed genes were observed (Table S1), validating our assumption that eCtrl is indeed equivalent to WT. Next, strict analysis criteria were used whereby gene expression levels in a

Figure 2. Directed differentiation of human iPSC lines with *FUS* P525L mutations and isogenic controls into MIGs

(A) Schematic of differentiation protocol of human iPSCs into MIGs.

(B) Phase-contrast images of iPSC-derived MIGs of different *FUS* genotypes. For time-lapse movies depicting motile pseudopodia and putative phagosomes, see Videos S1A and S1B.

(C) Flow cytometry dot plots of characteristic microglial surface markers in MIGs. FMO, fluorescence minus 1 control using WT cells.

(D) Immunocytochemistry of FUS and microglial protein TREM2 in MIGs. Scale bar, 50 μm. Presented here are clones from the AG line.

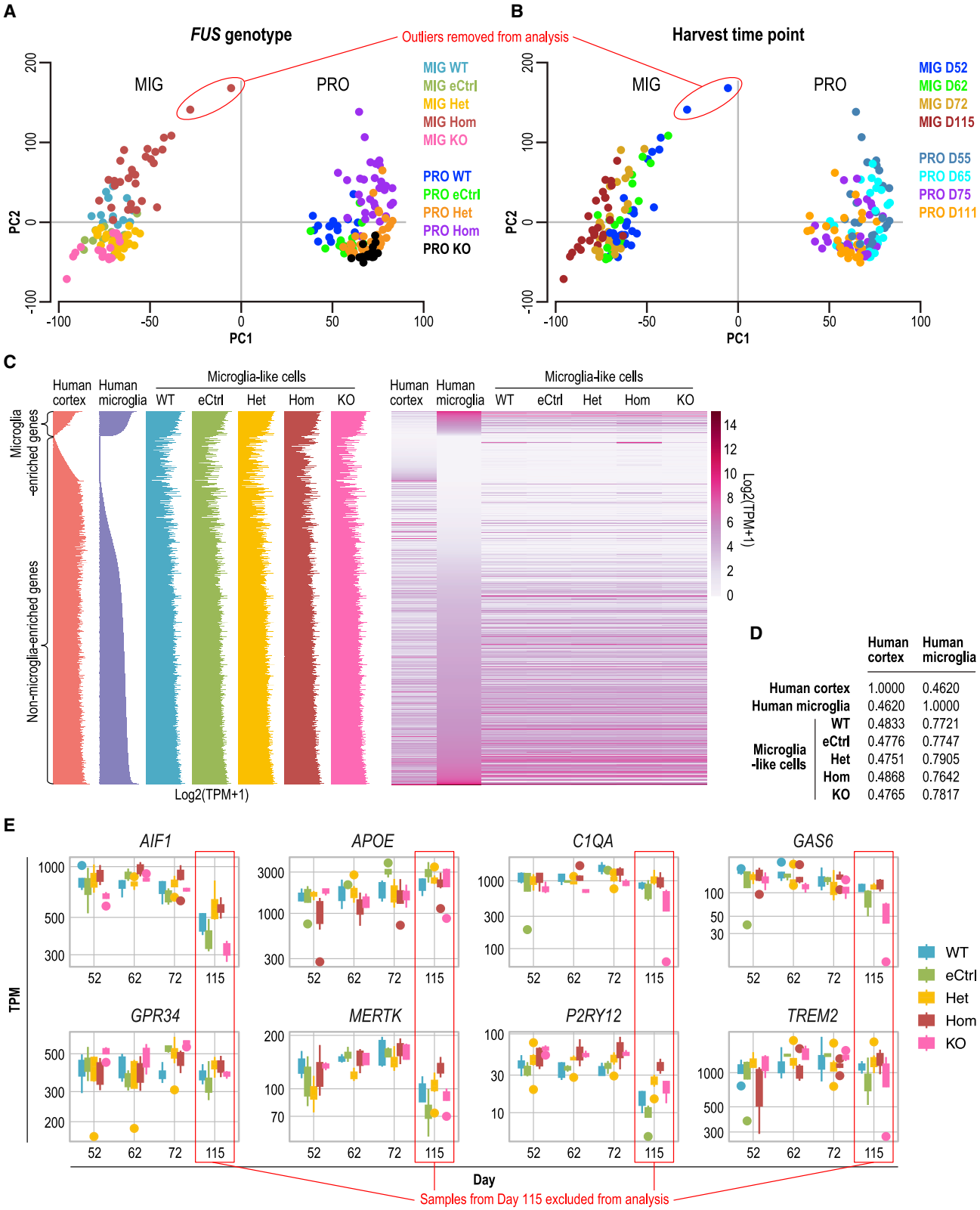

		Human cortex	Human microglia
Human cortex		1.0000	0.4620
Human microglia		0.4620	1.0000
Microglia-like cells	WT	0.4833	0.7721
	eCtrl	0.4776	0.7747
	Het	0.4751	0.7905
	Hom	0.4868	0.7642
	KO	0.4765	0.7817

(legend on next page)

mutant genotype were compared to those in WT or eCtrl independently, and only genes that were differentially expressed in the same direction against both controls were considered to be a mutant signature. Through this analysis, only 1 Het signature gene emerged (Table S1), which led us to postulate that the effects of P525L Het, if any, could be too weak for detection in this system.

Homozygous *FUS* P525L mutation may yield stronger and more experimentally robust phenotypes compared to heterozygotes due to dosage effects. By applying the same strict criteria, we detected a total of 120 differentially expressed genes in the MIG P525L Hom signature, whereby 90 were upregulated and 30 were downregulated (Figure 4D; Table S1). Gene Ontology (GO) enrichment analysis revealed that the Hom signature is enriched for genes associated with GO terms linked to inflammatory response, cell motility, chemotaxis, leukocyte migration, antigen processing and presentation, and cytokine production, which are characteristic features and functions of microglia (Figure 4E). However, analysis using the Molecular Signatures Database (MSigDB) with a focus on Canonical Pathways yielded "G protein-coupled receptor (GPCR) ligand binding" as the second top term with Hom signature gene enrichment (Figure S4A). Several of these GO and MSigDB categories share the same constituent genes (Table S2) and the differential expression levels of 20 of these genes were orthogonally validated using quantitative reverse transcriptase-PCR (qRT-PCR), the qualitative results of which corroborated those obtained via RNA-seq (Figure 4F; Table S3).

Differentially expressed chemoreceptor genes in MIGs with *FUS* P525L mutations lead to perturbations of ligand-induced intracellular calcium signaling

P2RY6, *GPR183*, *S1PR1*, and *CCR6* stood out as *FUS* P525L Hom signature genes encoding relatively well-studied G protein-coupled chemoreceptors with known biological ligands. The activation of P2RY6 by uridine diphosphate (UDP) nucleotides (Koizumi et al., 2007), GPR183 by 7α,25-dihydroxycholesterol (OHC) hydroxycholesterols (Preuss et al., 2014), sphingosine-1-phosphate receptor 1 (S1PR1) by S1P (Lee et al., 2017), and CCR6 by CCL20 (Liao et al., 2002) converge downstream on intracellular calcium flux, a common signal transduction pathway of GPCRs. To investigate whether the increased expression of these chemoreceptor genes in *FUS* P525L Hom MIGs translates into a functional phenotypic difference compared to WT and eCtrl, intracellular calcium flux assays were performed using the ligand of each receptor. We noted that our MIGs responded to UDP and 7α,25-OHC (Figures 5A and 5B), but no response to S1P and CCL20 was detected, even at high concentrations (Figures S5B and S5C).

Focusing on UDP and 7α,25-OHC, we proceeded to treat our MIGs of all 4 genotypes with these 2 ligands. Relative to WT and eCtrl, whose responses were not significantly different between the 2 as expected, intracellular calcium flux was significantly higher in P525L Hom when treated with UDP and 7α,25-OHC, respectively (Figures 5C and 5D). Despite not having a discernible differential gene expression signature, P525L Het cells also seemed to respond to UDP or 7α,25-OHC in terms of calcium flux compared to WT and eCtrl, albeit with a lower magnitude and less reliably compared to Hom. Calcium signals were greatly diminished when MRS2578 and NIBR189, potent specific inhibitors of P2RY6 and GPR183, respectively, were applied to the cells before ligand addition (Figures 5C and 5D). These findings were consistently reproduced in P525L Hom MIGs derived from both independent iPSC lines and across both independent differentiations. These observations signify that transcriptional perturbations due to *FUS* P525L mutant alleles in MIGs, causing *P2RY6* and *GPR183* gene expression upregulation, led to the disruption of intracellular calcium signaling downstream from the ligand activation of these chemoreceptors.

MIGs with *FUS* P525L mutations do not exhibit phagocytosis or cytokine release phenotypes

As opposed to their encounter with foreign pathogens, which triggers a large immune response, macrophages

Figure 3. Identity validation via RNA sequencing (RNA-seq) of iPSC-derived MIGs with *FUS* P525L mutations and isogenic controls.

(A and B) PCA of transcriptome profiles from RNA-seq of MIGs and their preceding myeloid progenitors (PRO). Color code indicates the different (A) *FUS* controls and P525L mutant genotypes or (B) time points of myeloid progenitor harvests in days (D) after differentiation initiation. The 2 outlier samples here are the same as those in the hierarchical clustering dendrogram (Figure S3B). PC, principal component.

(C) Transcriptome profile waterfall plots and heatmaps of MIGs of various *FUS* genotypes compared to those of purified human cortical microglia and brain cortex from Galatro et al. (2017). From top to bottom, microglia-enriched genes relative to brain cortex are arranged in decreasing order of expression level, followed by non-enriched genes in increasing order. See Table S4 for lists of microglia-enriched genes in primary human microglia and MIGs.

(D) Spearman's rank correlation coefficients calculated to compare the gene expression profiles of MIGs with, respectively, human primary microglia and brain cortex from Galatro et al. (2017).

(E) Box plots of gene expression level of microglial markers in MIGs across genotypes and time points at which myeloid progenitors were harvested for terminal differentiation. TPM, transcript per million. Presented here are clones from the AG line.

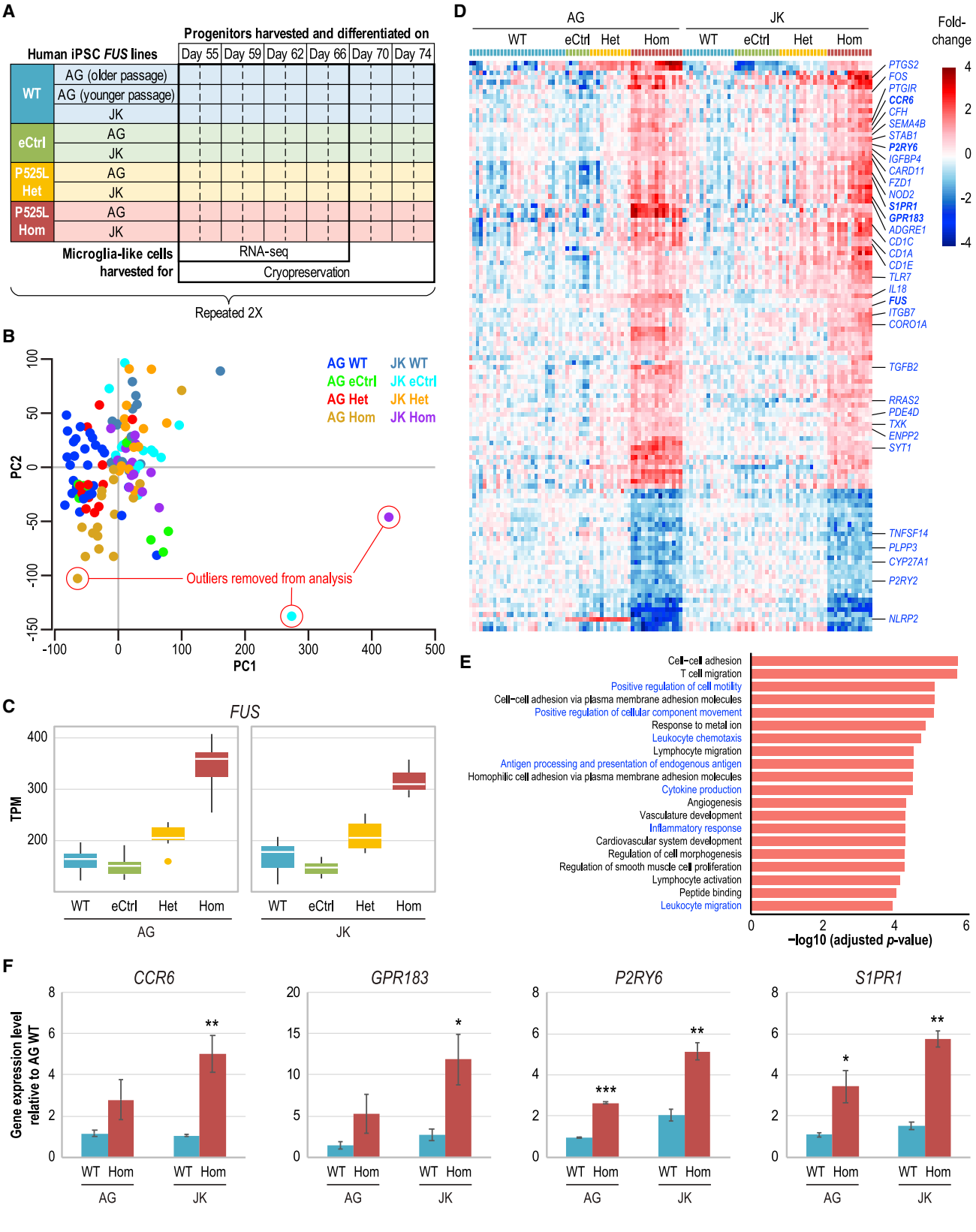

(legend on next page)

engulf dead cells in a relatively immunologically silent manner under homeostatic conditions, a process called efferocytosis (Green et al., 2016). Microglia, as the resident macrophage of the CNS, are tasked to phagocytose apoptotic cells and cellular debris such as myelin fragments. Microglial phagocytosis of dying neurons or degrading myelin has been linked to pathological conditions such as Alzheimer's disease, frontotemporal dementia, and multiple sclerosis (Prinz et al., 2019). With these contexts in mind, we established a live-cell imaging method that quantifies the uptake of apoptotic, commercially available, WT human iPSC-derived motor neurons to assay efferocytosis activity in our MIGs. While the MIGs of the *FUS* genotypic series were capable of phagocytosing apoptotic motor neurons, no dramatic differences were observed in efferocytosis activity in P525L Hom and Het compared to controls. Although a slight upregulated trend was noticeable in Hom compared to other genotypes, the variability across genotypes precluded any statistical significance (Figure 6A). Similarly, we established a myelin phagocytosis assay showing that our MIGs could phagocytose murine myelin fragments, although, again, the differences in activity across genotypes were not statistically significant (Figure S6A).

At the end of the 3-day phagocytosis assays, we collected the cell culture supernatants and profiled cytokines released by MIGs using the Luminex multiplex immunoassay platform. From a panel of 45 cytokines, only 8 were consistently detectable in MIGs, either when untreated or treated with apoptotic motor neurons or myelin. The levels of these detectable cytokines were not dramatically different across treatment conditions or genotypes. Although there may seem to be a trend for increased MIP-1α in *FUS* P525L Hom compared to controls (Figure S6B), this was not consistently reproducible in subsequent repeat experiments (data not shown). As a positive control, *Escherichia coli* was applied to the cells, which greatly increased the level of numerous cytokines (Figure S6C), reflecting very similar responses to bacterial lipopolysaccharide in other reported iPSC-derived microglia (Abud et al., 2017) or primary microglia (Rustenhoven et al., 2016). These results confirmed again that our differentiated cells do behave like microglia in their response to pathogens, matching their microglial molecular identity (Prinz et al., 2019).

Koizumi et al. (2007) have demonstrated that when cultured primary rat microglia were treated with exogenous UDP, their phagocytic activity was upregulated as mediated via the chemoreceptor P2RY6, while no chemotactic response was detected. Furthermore, when neuronal cell death was induced in the hippocampal regions of an *in vivo* rat model, the mRNA level of *P2RY6* was increased and the transcripts colocalized with adjacent activated microglia. Based on these findings and considering the upregulation of *P2RY6* in our *FUS* P525L Hom MIGs, UDP was applied to test its effect in our efferocytosis assay. Within the first 24 h of ligand application, an increase in phagocytic activity was seen in MIGs when compared to untreated controls across all genotypes, corroborating what was published by Koizumi and colleagues. However, no differential efferocytosis activities were evident in either P525L Het or Hom cells compared to controls (Figure 6B). In terms of cytokine profiling, UDP-mediated P2RY6 signaling has been shown to increase the level of cytokines such as IL-6, IL-8, macrophage inflammatory protein-1α (MIP-1α), and tumor necrosis factor-α (TNF-α) in a few myeloid cell culture models (Cox et al., 2005; Garcia et al., 2014; Kim et al., 2011). Although this effect of UDP was largely replicated in our

Figure 4. Homozygous *FUS* P525L MIGs display transcriptional perturbations of genes associated with characteristic microglial functions

(A) Experimental design for large-scale differentiation, RNA-seq, and cryopreservation of MIGs from independent AG and JK lines with various *FUS* control and P525L mutant genotypes. Each box represents a differentiation replicate.

(B) PCA of RNA-seq transcriptome profiles of MIGs differentiated from AG and JK lines with various *FUS* genotypes as represented by a color code. Two of the outlier samples here are the same as those in the hierarchical clustering dendrogram (Figure S4C); the third had been flagged as an outlier before RNA-seq due to its abnormal fibroblast-like morphology.

(C) Box plots of differential expression of the *FUS* gene in MIGs with different *FUS* genotypes as determined by RNA-seq.

(D) Heatmap of differentially expressed genes in *FUS* P525L Hom MIGs as compared independently to WT and Ctrl in both AG and JK lines. Each colored box at the very top represents a differentiation replicate. Displayed names in blue are those of genes associated with GO and MSigDB Canonical Pathways terms linked to microglial features and functions; in bold are GPCR genes selected for further functional studies and *FUS*. See Table S1 for a complete list of and more information on Hom signature genes.

(E) Top 20 GO terms associated with genes enriched in the P525L Hom signature. In blue are terms linked to characteristic features and functions of microglia. Red bars indicate that the majority of Hom signature genes associated with a term are upregulated. Multiple testing correction was performed using the Benjamini-Hochberg procedure to obtain adjusted p values. See Figure S4A and Table S2 for more gene enrichment analysis results.

(F) Validation via qRT-PCR of differentially expressed GPCR genes in the Hom signature. See Table S3 for more qRT-PCR validation results of Hom signature genes. Error bars represent standard deviations across the first 3 time points; n = 3.

*p < 0.05; **p < 0.01; ***p < 0.001.

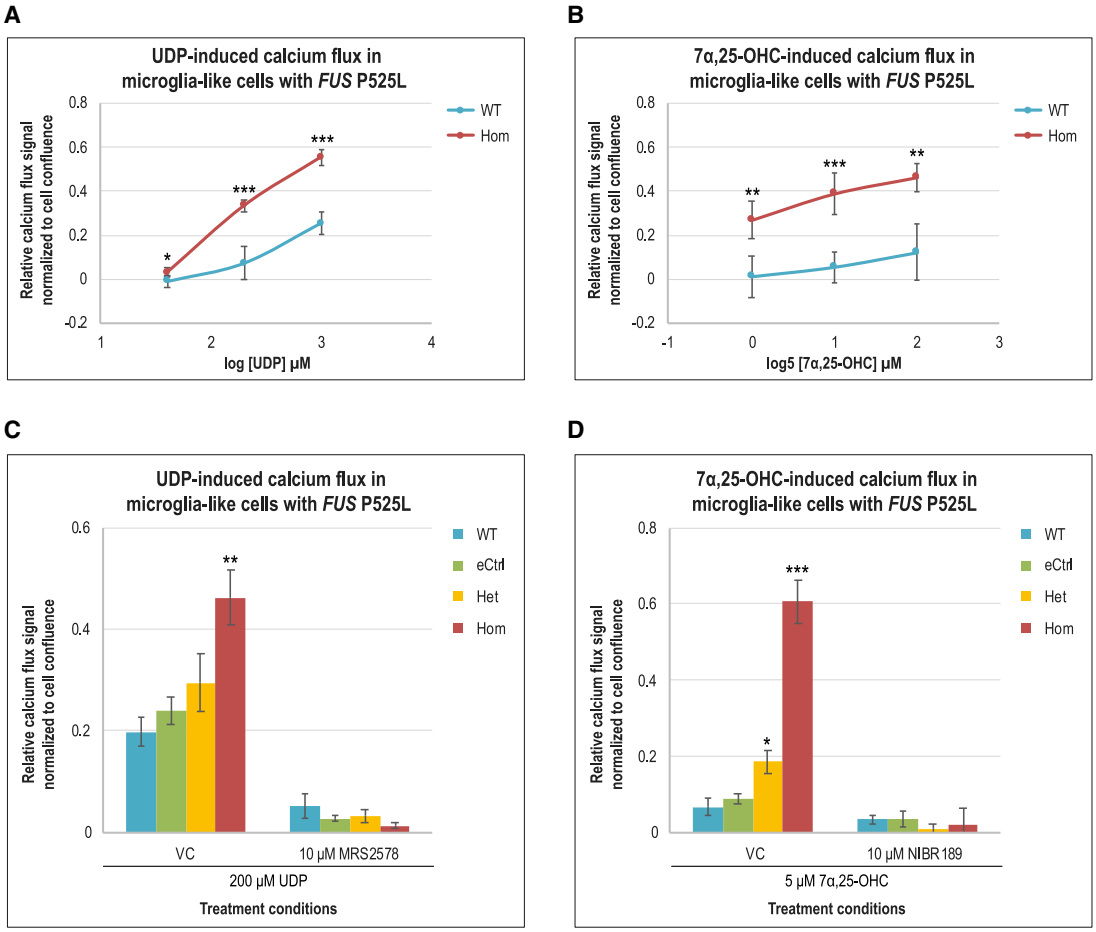

Figure 5. Differentially expressed chemoreceptor genes in MIGs with *FUS* P525L mutations lead to perturbations of ligand-induced intracellular calcium signaling

(A and B) Intracellular calcium response to increasing concentrations of (A) UDP or (B) 7α,25-OHC in WT and *FUS* P525L Hom MIGs.

(C and D) Intracellular calcium flux in response to (C) UDP or (D) 7α,25-OHC in MIGs of various genotypes. Respectively for the chemoreceptors P2RY6 and GPR183, MRS2578 and NIBR189 are potent specific inhibitors, while ddH_2O and DMSO serve as vehicle controls (VCs). Error bars represent standard errors of the mean across 3 independent experiments using both AG and JK lines; n = 3.

*p < 0.05; **p < 0.01; ***p < 0.001.

MIGs, no statistically significant differences were observed in cytokine release across the *FUS* genotypic series under UDP-treated conditions (Figure 6C). Lastly, we noted that despite being a signature gene of P525L Het and Hom MIGs, IL-18 could not be detected in all tested conditions (data not shown).

DISCUSSION

An increasing number of studies have highlighted the importance of the role that microglia play in neurodegenerative diseases such as ALS (Hickman et al., 2018). However, most of the research to understand microglial involvement uses mouse models overexpressing ALS-linked mutant proteins. In the case of *FUS*, mice overexpressing WT FUS (Mitchell et al., 2013) or an NLS-truncated version of the protein (Funikov et al., 2018) have demonstrated an activated microglia phenotype. Conditioned culture media from astrocytes overexpressing WT FUS were also shown to exacerbate pro-inflammatory cytokine production in primary cultures of rat microglia (Ajmone-Cat et al., 2019). Within the human context, the *FUS* P525L mutation has been studied in human iPSC-derived motor neurons where phenotypes such as FUS cytoplasmic mislocalization, FUS aggregation upon cellular stress, neuronal hypoexcitability, decreased synaptic activity, axonal transport defects, and disruption in DNA damage response signaling have been variously described (Guo et al., 2017; Lenzi et al., 2015; Wang et al., 2019). Despite these findings, questions

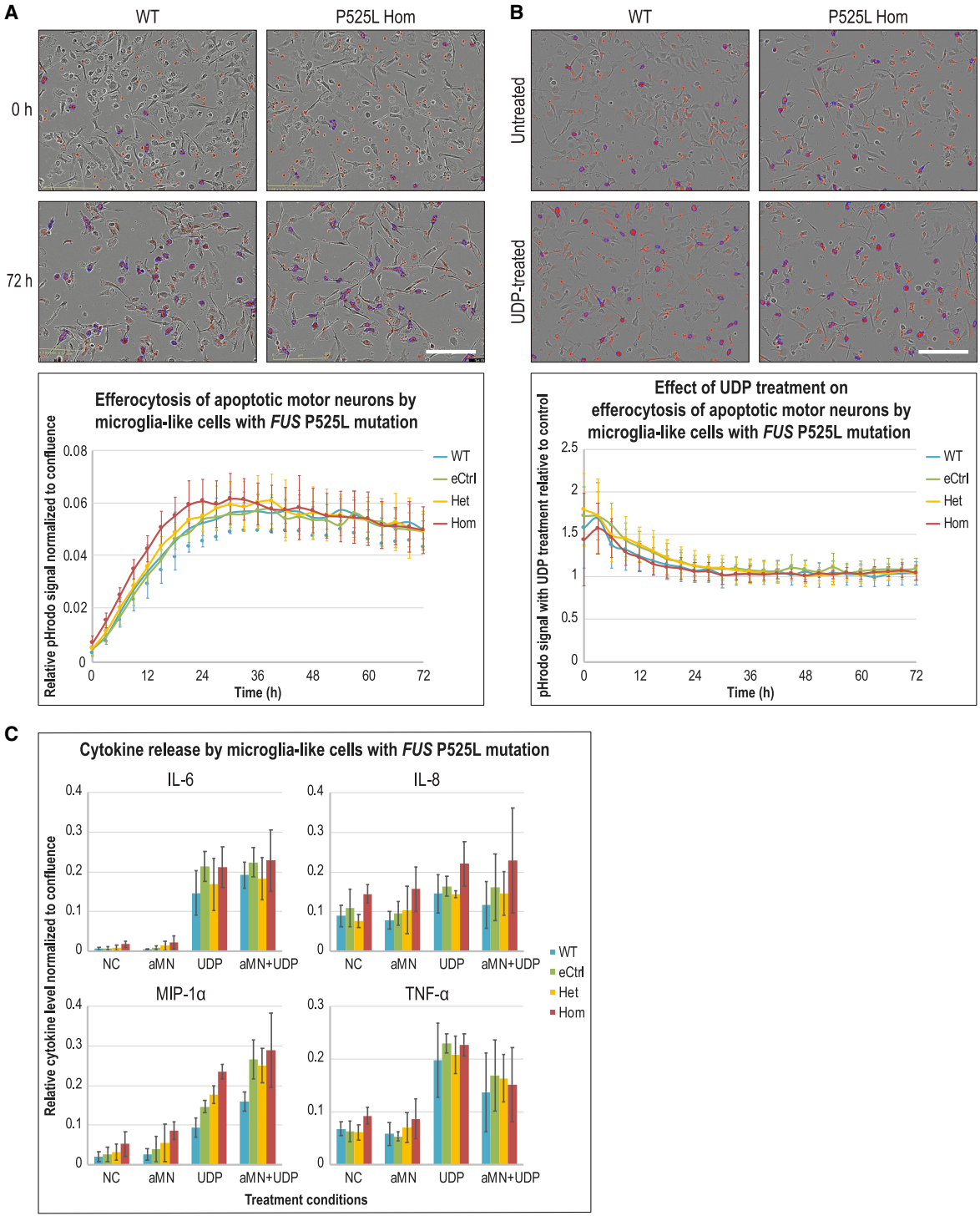

Figure 6. MIGs with *FUS* P525L mutations do not exhibit phagocytosis or cytokine release phenotypes

(A and B) Top half of each panel: Phase contrast and pHrodo red fluorescence overlay images of MIGs. pHrodo is a pH-sensitive dye that is almost non-fluorescent at neutral pH but fluoresces brightly (red for our assays) in acidic environments such as phagosomes. However, non-phagocytosed pHrodo-conjugated apoptotic motor neurons had high background fluorescence. To distinguish and exclude this background, efferocytosis activity was defined as pHrodo signals above a threshold area (represented by blue outline masks) because phagocytosed apoptotic motor neurons clustered together in phagosomes of MIGs. Due to space constraints, only representative images of

(legend continued on next page)

of whether and how ALS-linked *FUS* mutations at physiological levels affect human microglia in a cell-autonomous fashion remained unresolved. Our study bridges this knowledge gap.

We first established that human iPSCs carrying *FUS* P525L or complete KO mutations can be successfully differentiated into MIGs where FUS protein is mislocalized due to the P525L mutation. Proper microglial differentiation in the context of these mutations was not a given considering that *FUS* KO (Hicks et al., 2000) and homozygous P517L (the murine analog of P525L) knockin (Lyashchenko, 2015) mice die perinatally. We also report that while MIGs respond robustly to *E. coli* in regard to cytokine release, their response to apoptotic motor neurons or murine myelin fragments are seemingly rather muted. We surmise that this could reflect efferocytosis, the homeostatic function of phagocytes such as microglia in clearing up dead cells and debris in an immunologically silent manner (Green et al., 2016). As a technical note, we provide empirical evidence that MIGs differentiated from myeloid progenitors harvested between 50 and 75 days after differentiation initiation are highly comparable in terms of transcriptome profiles.

Our RNA-seq results clearly reveal that homozygous *FUS* P525L mutations perturb the transcriptome profile of MIGs. The P525L Hom signature is enriched for genes associated with several functional properties of microglia. In contrast to Hom, P525L Het MIGs do not exhibit significant transcriptional perturbations. Similarly, the downregulation of specific circular RNAs in iPSC-derived motor neurons observed by Errichelli et al. (2017) occurred in *FUS* P525L homozygotes but not in heterozygotes. This may not be entirely surprising because ALS symptoms caused by heterozygous *FUS* P525L mutation only arise after approximately a decade from birth, and these patients are not known to have congenital developmental defects (Kuang et al., 2017; Shang and Huang, 2016).

Guided by gene enrichment analyses, we focused on the *FUS* P525L Hom signature genes *P2RY6* and *GPR183* to probe whether their transcriptional upregulation translates into a functional alteration in MIGs. We confirmed that ligand activation of these 2 chemoreceptors does induce higher intracellular calcium flux signals in P525L Hom MIGs compared to controls. P2RY6 is activated by UDP released from damaged or dying cells (Anwar et al., 2020), and GPR183 is activated by 7α,25-OHC, a by-product of cholesterol catabolism (Kurschus and Wanke, 2018). These 2 chemoreceptors could be relevant to ALS since neuronal cell death and the breakdown of myelin, which is cholesterol rich, are characteristics of neurodegeneration. In fact, the pro-inflammatory activation of P2 receptors involving *P2RY6* upregulation in the ALS model of SOD1 G93A mutant murine microglia has been reported (D'Ambrosi et al., 2009). Inferring from research performed in other neurodegenerative diseases, we speculate that increased microglial P2RY6 and GPR183 signaling could initially play a protective role in ALS by promoting the phagocytosis of dying motor neurons and remyelination, but their prolonged activation would eventually lead to unresolved neuroinflammation and indiscriminate efferocytosis that exacerbates disease at later stages (Anwar et al., 2020; Klejbor et al., 2021).

In addition to *P2RY6*, a few other *FUS* P525L Hom signature genes in our MIGs have been implicated in ALS: *IL18*, *PTGS2*, *TGFB2*, and *TLR7*. The dysregulation of these genes occurs in ALS patients or SOD1 mutant mouse models of the disease and is mostly within the context of neuroinflammation (Berjaoui et al., 2015; Consilvio et al., 2004; Johann et al., 2015; Katsuno et al., 2011). Likewise, the FUS overexpression experiments in mouse or cell co-culture models mentioned previously also feature inflammatory activated microglia (Ajmone-Cat et al., 2019; Funikov et al., 2018; Mitchell et al., 2013). Many of these inflammation events have been shown or are likely to be due to microglial responses to neuronal death or other non-cell-autonomous interactions within complex environments. As contrasted in our simpler model, P525L Hom MIGs do not exhibit an overt activated phenotype in terms of increased phagocytosis or inflammatory cytokine release. Therefore, it would be interesting to investigate whether and how *FUS* P525L MIGs interact with other disease-relevant cell types via co-culture or *in vivo* transplantation experiments, which could uncover the relevance of our reported phenotypes to ALS pathogenesis.

Nonetheless, our discovery that homozygous *FUS* P525L mutations cell-autonomously perturb transcriptome profile and chemoreceptor signaling in a human microglia model has shed light on a previously unanswered question. Further research will be required to elucidate the specific mechanism by which homozygous P525L mutations cause

WT and *FUS* P525L Hom cells are displayed. Scale bar, 200 μm. Bottom half of each panel: (A) Graph for efferocytosis signal normalized to cell confluence versus time from live imaging of MIGs with different *FUS* genotypes. (B) Graph for efferocytosis signal in MIGs of various genotypes treated with UDP relative to signal in untreated control cells versus time. Error bars represent standard deviations across both AG and JK lines, each with 4 replicate wells; n = 8.

(C) Cytokine release of IL-6, IL-8, MIP-1α and TNF-α in cell culture supernatant by MIGs under different treatment conditions after 72 h. NC, untreated negative control; aMN, apoptotic motor neurons; UDP, 200 uM. Error bars represent standard deviations across both AG and JK lines, each with at least 2 replicate wells; n $\geq$ 4.

the phenotypes we have observed in human iPSC-derived microglia. The ability to reproducibly scale up microglial differentiation renders future biochemical studies possible to divulge any molecular interactions that could inform how pathological forms of FUS lead to altered microglial function.

EXPERIMENTAL PROCEDURES

See further details in the supplemental experimental procedures.

Differential gene expression analysis

Gene expressions were quantified from raw sequencing reads using the OmicSoft ArrayStudio RNA-seq analysis pipeline. Reads that uniquely mapped to the exons of a gene were identified and counted. The resulting read counts were summarized at the gene level as raw expression. Genes were flagged as "absent" or "present" in each sample using an empirical minimum raw read count of 10. For comparisons between 2 groups of samples, genes that were not flagged as present in all of the samples of the higher-expressing group were excluded. Differential gene expression levels were then analyzed using the DESeq2 method (Love et al., 2014). Briefly, raw read counts across samples were normalized to adjust for variation in sequencing depth. Dispersion of expression was estimated by sharing information across genes with similar expression levels and a negative binomial generalized linear model was constructed. Fold-change was computed as the effect size of the treatment, which reflects the difference in expression levels between 2 groups. The statistical significance of differential expression levels was assessed by the Wald test. Lastly, we defined genes with fold-changes of no less than 1.5 in either up or down direction with $p < 0.01$ as significantly perturbed gene signatures.

Intracellular calcium flux assay

MIGs were plated at 1×10^4 cells per well into flat clear-bottom black-walled poly-D-lysine-coated 96-well plates (Greiner, cat. no. 655946). At least 2 days later, an intracellular calcium flux assay was performed using the FLIPR Calcium 6 Assay Kit (Molecular Devices, cat. no. R8190) according to the manufacturer's protocol. Briefly, plated cells were incubated with calcium indicator dye containing 2.5 mM probenecid (Invitrogen, cat. no. P36400) for 2 h at 37 °C. When chemoreceptor inhibitors were used, they were applied at this step. Chemoreceptor ligands were prepared at the desired concentrations and aliquoted into V-bottom 96-deep well plates (Axygen, cat. no. P-96-450V-C-S). Assays were performed by measuring calcium indicator fluorescence intensity immediately upon ligand addition every second for 400 s on the FLIPR Tetra High-throughput Cellular Screening System with ICCD camera using ScreenWorks software (Molecular Devices). See the supplemental experimental procedures for more detailed information.

Data and code availability

The accession number for the RNA-seq datasets generated in this paper is GEO: GSE172459. The datasets from Galatro et al. are available through GEO: GSE99074.

SUPPLEMENTAL INFORMATION

Supplemental information can be found online at https://doi.org/10.1016/j.stemcr.2022.01.004.

AUTHOR CONTRIBUTIONS

Conceptualization, S.Y.K. and E.C.; methodology, S.Y.K., E.C., C.H., and J.K.; software, Y.B.; investigation, S.Y.K., J.S., P.L., J.N., K.L., N.C., A.C., Q.T., J.E., H.J., and C.F.; data curation, S.Y.K. and Y.B.; formal analysis, S.Y.K., Y.B., and T.Y.; validation, S.Y.K.; visualization, S.Y.K. and Y.B.; writing – original draft, S.Y.K.; writing – review & editing, S.Y.K., E.C., and B.Z.; supervision, E.C., B.Z., S.Y.K., and Y.B.

CONFLICTS OF INTERESTS

All of the authors are current or former employees of Regeneron Pharmaceuticals.

ACKNOWLEDGMENTS

We thank Meghan Drummond for providing expertise in CRISPR reagent design, Daria Zamolodchikov for providing the pHrodo-conjugated murine myelin fragment reagent, and many of our colleagues in Velocigene and across Regeneron for making this project possible. We also thank Drummond and Zamolodchikov again, as well as Kevin Kanning and Aarti Sharma for providing insightful comments on the manuscript.

Received: April 28, 2021
Revised: January 5, 2022
Accepted: January 6, 2022
Published: March 8, 2022

REFERENCES

Abud, E.M., Ramirez, R.N., Martinez, E.S., Healy, L.M., Nguyen, C.H.H., Newman, S.A., Yeromin, A.V., Scarfone, V.M., Marsh, S.E., Fimbres, C., et al. (2017). iPSC-derived human microglia-like cells to study neurological diseases. Neuron *94*, 278–293.e9.

Ajmone-Cat, M.A., Onori, A., Toselli, C., Stronati, E., Morlando, M., Bozzoni, I., Monni, E., Kokaia, Z., Lupo, G., Minghetti, L., et al. (2019). Increased FUS levels in astrocytes leads to astrocyte and microglia activation and neuronal death. Sci. Rep. *9*, 4572.

Anwar, S., Pons, V., and Rivest, S. (2020). Microglia purinoceptor P2Y6: an emerging therapeutic target in CNS diseases. Cells *9*, 1595.

Bennett, M.L., Bennett, F.C., Liddelow, S.A., Ajami, B., Zamanian, J.L., Fernhoff, N.B., Mulinyawe, S.B., Bohlen, C.J., Adil, A., Tucker, A., et al. (2016). New tools for studying microglia in the mouse and human CNS. Proc. Natl. Acad. Sci. U S A. *113*, E1738–E1746.

Berjaoui, S., Povedano, M., Garcia-Esparcia, P., Carmona, M., Aso, E., and Ferrer, I. (2015). Complex inflammation mRNA-related response in ALS is region dependent. Neural Plast. *2015*, 573784.

Butovsky, O., Jedrychowski, M.P., Moore, C.S., Cialic, R., Lanser, A.J., Gabriely, G., Koeglsperger, T., Dake, B., Wu, P.M., Doykan, C.E., et al. (2014). Identification of a unique TGF-beta-dependent

molecular and functional signature in microglia. Nat. Neurosci. *17*, 131–143.

Clarke, B.E., and Patani, R. (2020). The microglial component of amyotrophic lateral sclerosis. Brain *143*, 3526–3539.

Consilvio, C., Vincent, A.M., and Feldman, E.L. (2004). Neuroinflammation, COX-2, and ALS–a dual role? Exp. Neurol. *187*, 1–10.

Cox, M.A., Gomes, B., Palmer, K., Du, K., Wiekowski, M., Wilburn, B., Petro, M., Chou, C.C., Desquitado, C., Schwarz, M., et al. (2005). The pyrimidinergic P2Y6 receptor mediates a novel release of proinflammatory cytokines and chemokines in monocytic cells stimulated with UDP. Biochem. Biophys. Res. Commun. *330*, 467–473.

D'Ambrosi, N., Finocchi, P., Apolloni, S., Cozzolino, M., Ferri, A., Padovano, V., Pietrini, G., Carri, M.T., and Volonte, C. (2009). The proinflammatory action of microglial P2 receptors is enhanced in SOD1 models for amyotrophic lateral sclerosis. J. Immunol. *183*, 4648–4656.

Douvaras, P., Sun, B., Wang, M., Kruglikov, I., Lallos, G., Zimmer, M., Terrenoire, C., Zhang, B., Gandy, S., Schadt, E., et al. (2017). Directed differentiation of human pluripotent stem cells to microglia. Stem Cell Rep. *8*, 1516–1524.

Errichelli, L., Dini Modigliani, S., Laneve, P., Colantoni, A., Legnini, I., Capauto, D., Rosa, A., De Santis, R., Scarfo, R., Peruzzi, G., et al. (2017). FUS affects circular RNA expression in murine embryonic stem cell-derived motor neurons. Nat Commun *8*, 14741.

Funikov, S.Y., Rezvykh, A.P., Mazin, P.V., Morozov, A.V., Maltsev, A.V., Chicheva, M.M., Vikhareva, E.A., Evgen'ev, M.B., and Ustyugov, A.A. (2018). FUS(1-359) transgenic mice as a model of ALS: pathophysiological and molecular aspects of the proteinopathy. Neurogenetics *19*, 189–204.

Galatro, T.F., Holtman, I.R., Lerario, A.M., Vainchtein, I.D., Brouwer, N., Sola, P.R., Veras, M.M., Pereira, T.F., Leite, R.E.P., Moller, T., et al. (2017). Transcriptomic analysis of purified human cortical microglia reveals age-associated changes. Nat. Neurosci. *20*, 1162–1171.

Garcia, R.A., Yan, M., Search, D., Zhang, R., Carson, N.L., Ryan, C.S., Smith-Monroy, C., Zheng, J., Chen, J., Kong, Y., et al. (2014). P2Y6 receptor potentiates pro-inflammatory responses in macrophages and exhibits differential roles in atherosclerotic lesion development. PLoS One *9*, e111385.

Ginhoux, F., Lim, S., Hoeffel, G., Low, D., and Huber, T. (2013). Origin and differentiation of microglia. Front Cell Neurosci *7*, 45.

Gosselin, D., Skola, D., Coufal, N.G., Holtman, I.R., Schlachetzki, J.C.M., Sajti, E., Jaeger, B.N., O'Connor, C., Fitzpatrick, C., Pasillas, M.P., et al. (2017). An environment-dependent transcriptional network specifies human microglia identity. Science *356*, eaal3222.

Green, D.R., Oguin, T.H., and Martinez, J. (2016). The clearance of dying cells: table for two. Cell Death Differ *23*, 915–926.

Guo, W., Naujock, M., Fumagalli, L., Vandoorne, T., Baatsen, P., Boon, R., Ordovas, L., Patel, A., Welters, M., Vanwelden, T., et al. (2017). HDAC6 inhibition reverses axonal transport defects in motor neurons derived from FUS-ALS patients. Nat. Commun. *8*, 861.

Hickman, S., Izzy, S., Sen, P., Morsett, L., and El Khoury, J. (2018). Microglia in neurodegeneration. Nat. Neurosci. *21*, 1359–1369.

Hickman, S.E., Kingery, N.D., Ohsumi, T.K., Borowsky, M.L., Wang, L.C., Means, T.K., and El Khoury, J. (2013). The microglial sensome revealed by direct RNA sequencing. Nat. Neurosci. *16*, 1896–1905.

Hicks, G.G., Singh, N., Nashabi, A., Mai, S., Bozek, G., Klewes, L., Arapovic, D., White, E.K., Koury, M.J., Oltz, E.M., et al. (2000). Fus deficiency in mice results in defective B-lymphocyte development and activation, high levels of chromosomal instability and perinatal death. Nat. Genet. *24*, 175–179.

Ji, A.L., Zhang, X., Chen, W.W., and Huang, W.J. (2017). Genetics insight into the amyotrophic lateral sclerosis/frontotemporal dementia spectrum. J. Med. Genet. *54*, 145–154.

Johann, S., Heitzer, M., Kanagaratnam, M., Goswami, A., Rizo, T., Weis, J., Troost, D., and Beyer, C. (2015). NLRP3 inflammasome is expressed by astrocytes in the SOD1 mouse model of ALS and in human sporadic ALS patients. Glia *63*, 2260–2273.

Katsuno, M., Adachi, H., Banno, H., Suzuki, K., Tanaka, F., and Sobue, G. (2011). Transforming growth factor-beta signaling in motor neuron diseases. Curr. Mol. Med. *11*, 48–56.

Kim, B., Jeong, H.K., Kim, J.H., Lee, S.Y., Jou, I., and Joe, E.H. (2011). Uridine 5′-diphosphate induces chemokine expression in microglia and astrocytes through activation of the P2Y6 receptor. J. Immunol. *186*, 3701–3709.

Klejbor, I., Shimshek, D.R., Klimaszewska-Lata, J., Velasco-Estevez, M., Morys, J., Karaszewski, B., Szutowicz, A., and Rutkowska, A. (2021). EBI2 is expressed in glial cells in multiple sclerosis lesions, and its knock-out modulates remyelination in the cuprizone model. Eur. J. Neurosci. *54*, 5173–5188.

Koizumi, S., Shigemoto-Mogami, Y., Nasu-Tada, K., Shinozaki, Y., Ohsawa, K., Tsuda, M., Joshi, B.V., Jacobson, K.A., Kohsaka, S., and Inoue, K. (2007). UDP acting at P2Y6 receptors is a mediator of microglial phagocytosis. Nature *446*, 1091–1095.

Kuang, L., Kamelgarn, M., Arenas, A., Gal, J., Taylor, D., Gong, W., Brown, M., St Clair, D., Kasarskis, E.J., and Zhu, H. (2017). Clinical and experimental studies of a novel P525R FUS mutation in amyotrophic lateral sclerosis. Neurol. Genet. *3*, e172.

Kurschus, F.C., and Wanke, F. (2018). EBI2 - sensor for dihydroxycholesterol gradients in neuroinflammation. Biochimie *153*, 52–55.

Lavin, Y., Winter, D., Blecher-Gonen, R., David, E., Keren-Shaul, H., Merad, M., Jung, S., and Amit, I. (2014). Tissue-resident macrophage enhancer landscapes are shaped by the local microenvironment. Cell *159*, 1312–1326.

Lee, M.H., Appleton, K.M., El-Shewy, H.M., Sorci-Thomas, M.G., Thomas, M.J., Lopes-Virella, M.F., Luttrell, L.M., Hammad, S.M., and Klein, R.L. (2017). S1P in HDL promotes interaction between SR-BI and S1PR1 and activates S1PR1-mediated biological functions: calcium flux and S1PR1 internalization. J. Lipid Res. *58*, 325–338.

Lenzi, J., De Santis, R., de Turris, V., Morlando, M., Laneve, P., Calvo, A., Caliendo, V., Chio, A., Rosa, A., and Bozzoni, I. (2015). ALS mutant FUS proteins are recruited into stress granules in induced pluripotent stem cell-derived motoneurons. Dis. Model Mech. *8*, 755–766.

Li, Q., and Barres, B.A. (2018). Microglia and macrophages in brain homeostasis and disease. Nat. Rev. Immunol. *18*, 225–242.

Liao, F., Shirakawa, A.K., Foley, J.F., Rabin, R.L., and Farber, J.M. (2002). Human B cells become highly responsive to macrophage-inflammatory protein-3 alpha/CC chemokine ligand-20 after cellular activation without changes in CCR6 expression or ligand binding. J. Immunol. *168*, 4871–4880.

Lo Bello, M., Di Fini, F., Notaro, A., Spataro, R., Conforti, F.L., and La Bella, V. (2017). ALS-related mutant FUS protein is mislocalized to cytoplasm and is recruited into stress granules of fibroblasts from asymptomatic FUS P525L mutation carriers. Neurodegener Dis. *17*, 292–303.

Love, M.I., Huber, W., and Anders, S. (2014). Moderated estimation of fold change and dispersion for RNA-seq data with DESeq2. Genome Biol. *15*, 550.

Lyashchenko, A.K. (2015). Mechanisms of FUS-Mediated Motor Neuron Degeneration in Amyotrophic Lateral Sclerosis (Columbia University).

Mitchell, J.C., McGoldrick, P., Vance, C., Hortobagyi, T., Sreedharan, J., Rogelj, B., Tudor, E.L., Smith, B.N., Klasen, C., Miller, C.C., et al. (2013). Overexpression of human wild-type FUS causes progressive motor neuron degeneration in an age- and dose-dependent fashion. Acta Neuropathol. *125*, 273–288.

Muffat, J., Li, Y., Yuan, B., Mitalipova, M., Omer, A., Corcoran, S., Bakiasi, G., Tsai, L.H., Aubourg, P., Ransohoff, R.M., et al. (2016). Efficient derivation of microglia-like cells from human pluripotent stem cells. Nat. Med. *22*, 1358–1367.

Naumann, M., Peikert, K., Gunther, R., van der Kooi, A.J., Aronica, E., Hubers, A., Danel, V., Corcia, P., Pan-Montojo, F., Cirak, S., et al. (2019). Phenotypes and malignancy risk of different FUS mutations in genetic amyotrophic lateral sclerosis. Ann. Clin. Transl Neurol. *6*, 2384–2394.

Pandya, H., Shen, M.J., Ichikawa, D.M., Sedlock, A.B., Choi, Y., Johnson, K.R., Kim, G., Brown, M.A., Elkahloun, A.G., Maric, D., et al. (2017). Differentiation of human and murine induced pluripotent stem cells to microglia-like cells. Nat. Neurosci. *20*, 753–759.

Portz, B., Lee, B.L., and Shorter, J. (2021). FUS and TDP-43 phases in health and disease. Trends Biochem. Sci. *46*, 550–563.

Preuss, I., Ludwig, M.G., Baumgarten, B., Bassilana, F., Gessier, F., Seuwen, K., and Sailer, A.W. (2014). Transcriptional regulation and functional characterization of the oxysterol/EBI2 system in primary human macrophages. Biochem. Biophys. Res. Commun. *446*, 663–668.

Prinz, M., Jung, S., and Priller, J. (2019). Microglia biology: one century of evolving concepts. Cell *179*, 292–311.

Rustenhoven, J., Park, T.I., Schweder, P., Scotter, J., Correia, J., Smith, A.M., Gibbons, H.M., Oldfield, R.L., Bergin, P.S., Mee, E.W., et al. (2016). Isolation of highly enriched primary human microglia for functional studies. Sci. Rep. *6*, 19371.

Shang, Y., and Huang, E.J. (2016). Mechanisms of FUS mutations in familial amyotrophic lateral sclerosis. Brain Res. *1647*, 65–78.

Souza, P.V., Pinto, W.B., Chieia, M.A., and Oliveira, A.S. (2015). Clinical and genetic basis of familial amyotrophic lateral sclerosis. Arq Neuropsiquiatr *73*, 1026–1037.

Taylor, J.P., Brown, R.H., Jr., and Cleveland, D.W. (2016). Decoding ALS: from genes to mechanism. Nature *539*, 197–206.

Tyzack, G.E., Luisier, R., Taha, D.M., Neeves, J., Modic, M., Mitchell, J.S., Meyer, I., Greensmith, L., Newcombe, J., Ule, J., et al. (2019). Widespread FUS mislocalization is a molecular hallmark of amyotrophic lateral sclerosis. Brain *142*, 2572–2580.

Wang, H., Rangaswamy, S., Kodavati, M., Mitra, J., Guo, W., Guerrero, E.N., Van Den Bosch, L., and Hegde, M.L. (2019). RT(2) PCR array screening reveals distinct perturbations in DNA damage response signaling in FUS-associated motor neuron disease. Mol. Brain *12*, 103.

Wang, Y., Szretter, K.J., Vermi, W., Gilfillan, S., Rossini, C., Cella, M., Barrow, A.D., Diamond, M.S., and Colonna, M. (2012). IL-34 is a tissue-restricted ligand of CSF1R required for the development of Langerhans cells and microglia. Nat. Immunol. *13*, 753–760.

Weisheit, I., Kroeger, J.A., Malik, R., Klimmt, J., Crusius, D., Dannert, A., Dichgans, M., and Paquet, D. (2020). Detection of deleterious on-target effects after HDR-mediated CRISPR editing. Cell Rep *31*, 107689.

Xu, D., Jin, T., Zhu, H., Chen, H., Ofengeim, D., Zou, C., Mifflin, L., Pan, L., Amin, P., Li, W., et al. (2018). TBK1 suppresses RIPK1-driven apoptosis and inflammation during development and in aging. Cell *174*, 1477–1491.

Yang, L., Zhang, J., Kamelgarn, M., Niu, C., Gal, J., Gong, W., and Zhu, H. (2015). Subcellular localization and RNAs determine FUS architecture in different cellular compartments. Hum. Mol. Genet. *24*, 5174–5183.

Zhang, Y., Sloan, S.A., Clarke, L.E., Caneda, C., Plaza, C.A., Blumenthal, P.D., Vogel, H., Steinberg, G.K., Edwards, M.S., Li, G., et al. (2016). Purification and characterization of progenitor and mature human astrocytes reveals transcriptional and functional differences with mouse. Neuron *89*, 37–53.

Zhou, Y., Liu, S., Liu, G., Ozturk, A., and Hicks, G.G. (2013). ALS-associated FUS mutations result in compromised FUS alternative splicing and autoregulation. PLoS Genet. *9*, e1003895.

Stem Cell Reports, Volume *17*

Supplemental Information

Homozygous ALS-linked *FUS* P525L mutations cell- autonomously perturb transcriptome profile and chemoreceptor signaling in human iPSC microglia

Sze Yen Kerk, Yu Bai, Janell Smith, Pranav Lalgudi, Charleen Hunt, Junko Kuno, John Nuara, Tao Yang, Kathryn Lanza, Newton Chan, Angel Coppola, Qian Tang, Jennifer Espert, Henderson Jones, Casey Fannell, Brian Zambrowicz, and Eric Chiao

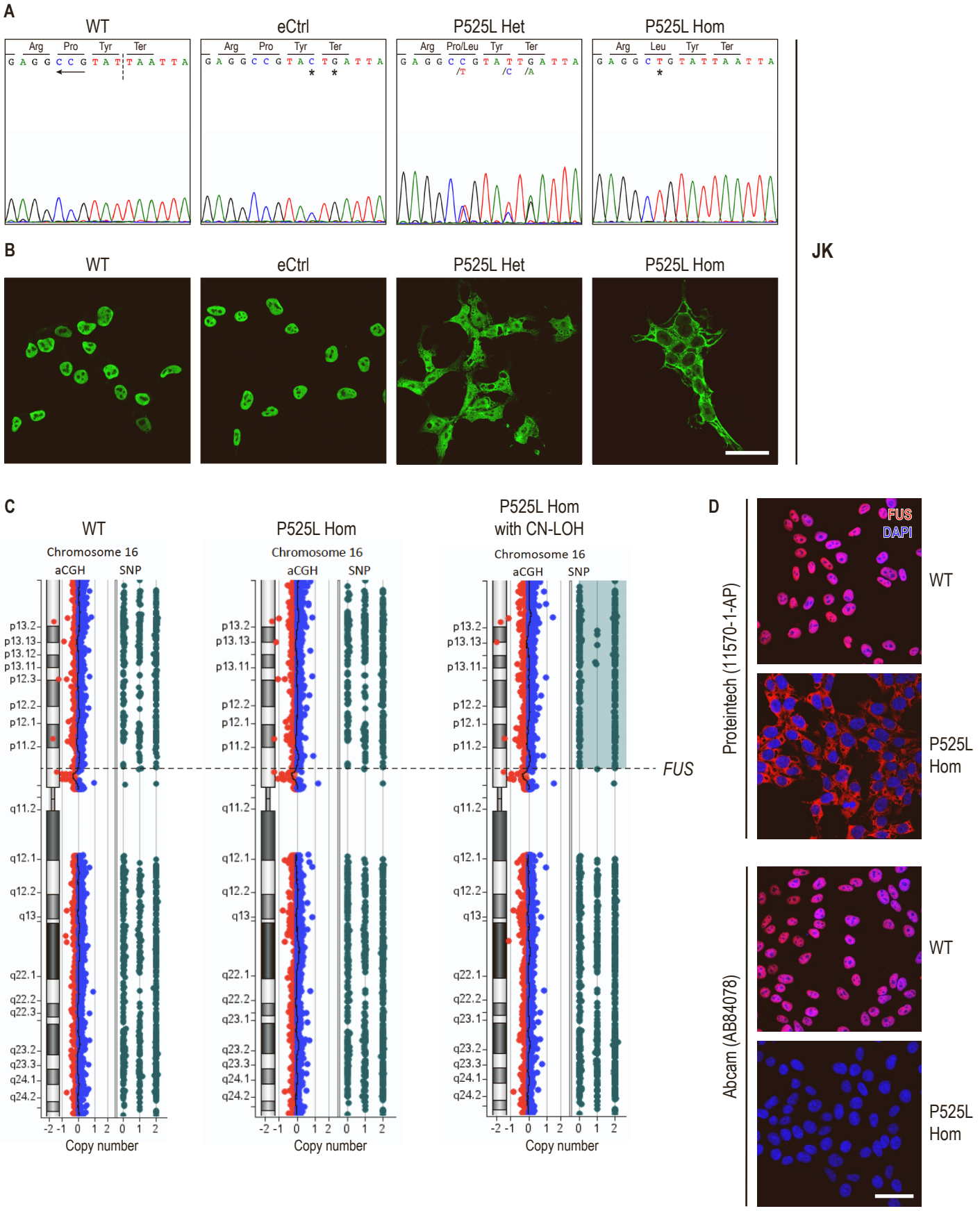
A
WT
eCtrl
P525L Het
P525L Hom
Arg Pro Tyr Ter
G A G G C C G T A T T A A T T A
Arg Pro Tyr Ter
G A G G C C G T A C T G A T T A
Arg Pro/Leu Tyr Ter
G A G G C C G T A T T G A T T A
/T /C /A
Arg Leu Tyr Ter
G A G G C T G T A T T A A T T A
B
WT
eCtrl
P525L Het
P525L Hom
JK
C
WT
P525L Hom
P525L Hom with CN-LOH
Chromosome 16
aCGH
SNP
p13.2
p13.13
p13.12
p13.11
p12.3
p12.2
p12.1
p11.2
q11.2
q12.1
q12.2
q13
q22.1
q22.2
q22.3
q23.1
q23.2
q23.3
q24.1
q24.2
FUS
-2 -1 0 1 2 0 1 2
Copy number
D
Proteintech (11570-1-AP)
Abcam (AB84078)
FUS
DAPI
WT
P525L Hom
WT
P525L Hom

Figure S1. CRISPR engineering of *FUS* P525L mutations and isogenic controls in independent human iPSC lines. Related to Figure 1.

(A) Sanger sequencing of CRISPR-engineered *FUS* genomic locus in human iPSC lines. In the WT panel, the inverted NGG PAM site is underlined by the arrow whereas the Cas9 endonuclease cut site is bisected by the perforated line. Homozygous point mutations compared to WT, such as that in P525L Hom, are denoted by asterisks (*). Heterozygous point mutations such as those in P525L Het are denoted by a slash (/) followed by the mutant allele.

(B) Immunocytochemistry of FUS protein revealing its subcellular localization in iPSCs of different genotypes. To better visualize the cytoplasmic compartment, iPSCs were single-cellularly dissociated and treated with ROCK inhibitor Y-27632 which causes cells to stretch out on the culture surface.

(C) aCGH and SNP microarray results of iPSC clones with WT and P525L Hom genotypes. Balanced red and blue aCGH signals centered at 0 copy number indicate no gross karyotypic abnormalities such as large genomic sequence amplications or deletions. Balanced distribution of green SNP signals across 0, 1, 2 copy numbers denotes normal SNP distributions. Shaded green region with SNP signals missing from 1 copy number signify CN-LOH across entire chromosome arm.

(D) As a technical note, we report that the Abcam antibody seemed to recognize only WT FUS but not P525L whereas the Proteintech antibody recognized both protein isoforms. The immunogen for the Abcam antibody is amino acids 1-50 of human FUS whereas that for the Proteintech antibody is amino acids 52-400 of human FUS. We hypothesize that P525L changes the 3-dimensional structure of FUS is a way that renders the Abcam antibody epitope unrecognizable but does not affect that of Proteintech.

Scale bar = 50 μm.

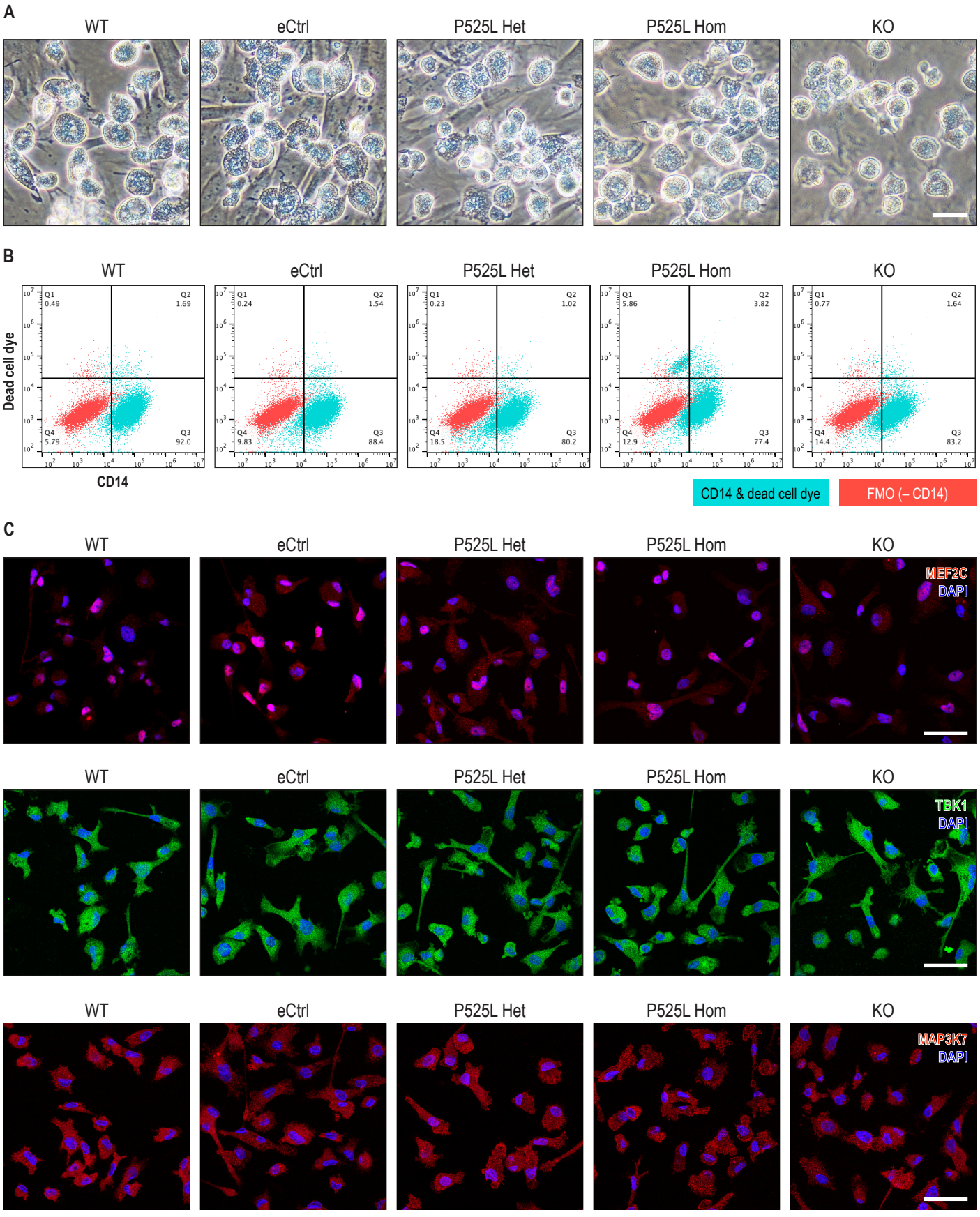
A
WT
eCtrl
P525L Het
P525L Hom
KO
B
WT
eCtrl
P525L Het
P525L Hom
KO
Dead cell dye
CD14
Q1 0.49
Q2 1.69
Q4 5.79
Q3 92.0
Q1 0.24
Q2 1.54
Q4 9.83
Q3 88.4
Q1 0.23
Q2 1.02
Q4 18.5
Q3 80.2
Q1 5.86
Q2 3.82
Q4 12.9
Q3 77.4
Q1 0.77
Q2 1.64
Q4 14.4
Q3 83.2
CD14 & dead cell dye
FMO (– CD14)
C
WT
eCtrl
P525L Het
P525L Hom
KO
MEF2C
DAPI
TBK1
DAPI
MAP3K7
DAPI

Figure S2. Differentiation of human iPSC lines with *FUS* P525L mutations and isogenic controls into MIGs. Related to Figure 2.

(A) Phase contrast images of iPSC-derived myeloid progenitor cells of different *FUS* genotypes.

(B) Flow cytometry dot plots of characteristic myeloid progenitor surface marker CD14 as well as a dead cell dye to indicate viability in myeloid progenitor cells. FMO: fluorescence minus one control using WT cells.

(C) Immunocytochemistry of additional microglia proteins in iPSC-derived MIGs of different *FUS* genotypes.

Scale bar = 50 μm. Presented here are clones from the AG line.

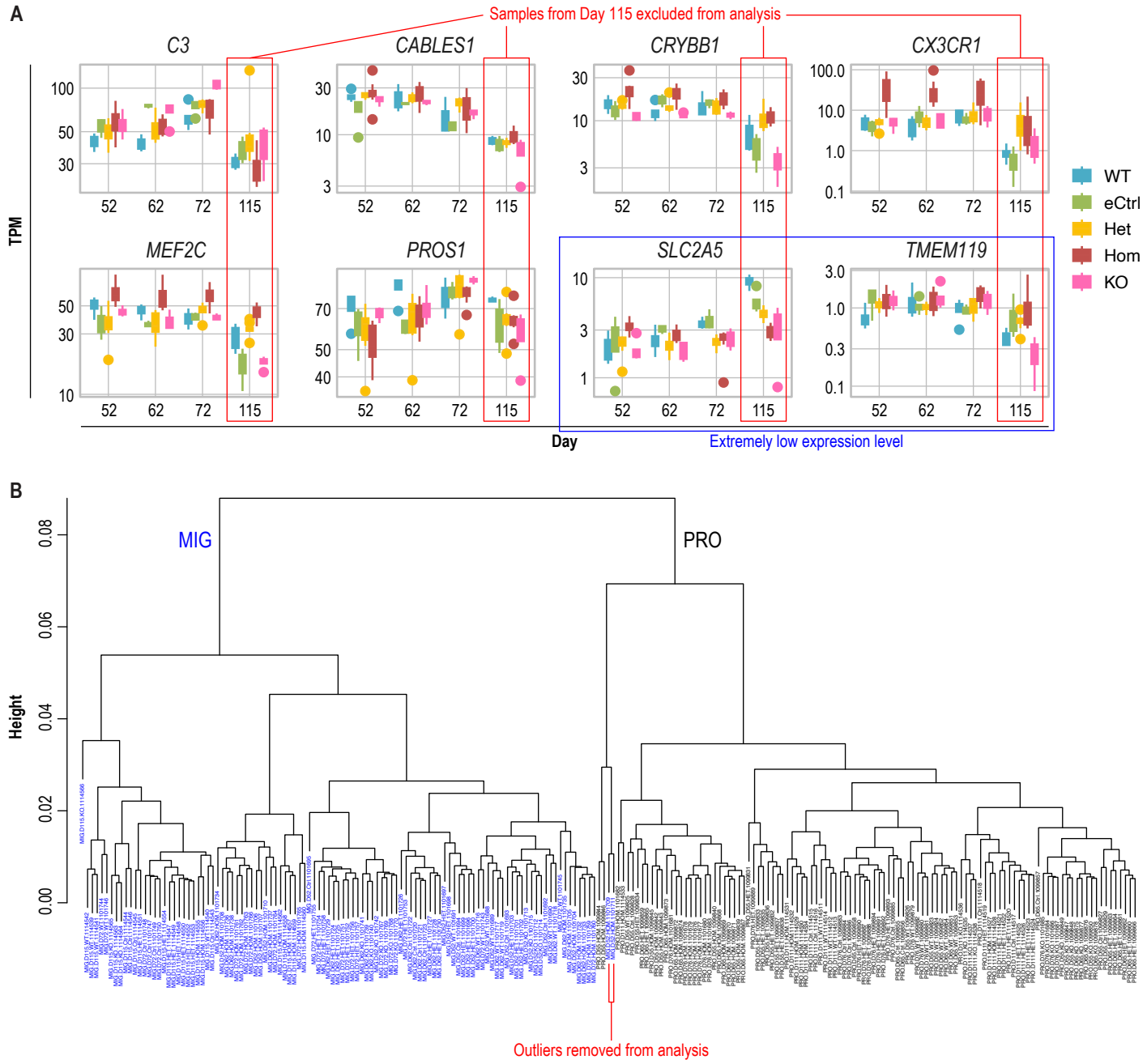
A
Samples from Day 115 excluded from analysis
C3
CABLES1
CRYBB1
CX3CR1
MEF2C
PROS1
SLC2A5
TMEM119
TPM
Day
Extremely low expression level
WT
eCtrl
Het
Hom
KO
B
MIG
PRO
Height
Outliers removed from analysis

Figure S3. Identity validation via RNA sequencing of iPSC-derived MIGs with *FUS* P525L mutations and isogenic controls. Related to Figure 3.

(A) Box plots of gene expression level of microglial markers in MIGs across genotypes and time points at which myeloid progenitors were harvested for terminal differentiation. TPM: transcript per million. Presented here are clones from the AG line.

(B) Hierarchical clustering of transcriptome profiles from RNA-seq of MIGs and their preceding PROs. The two outlier samples here are the same as those in the PCA plot (**Figure 3A** and **3B**).

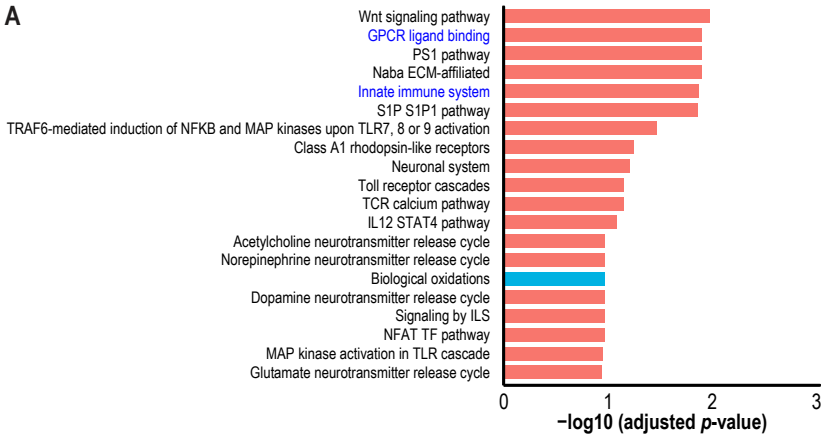
A
Wnt signaling pathway
GPCR ligand binding
PS1 pathway
Naba ECM-affiliated
Innate immune system
S1P S1P1 pathway
TRAF6-mediated induction of NFKB and MAP kinases upon TLR7, 8 or 9 activation
Class A1 rhodopsin-like receptors
Neuronal system
Toll receptor cascades
TCR calcium pathway
IL12 STAT4 pathway
Acetylcholine neurotransmitter release cycle
Norepinephrine neurotransmitter release cycle
Biological oxidations
Dopamine neurotransmitter release cycle
Signaling by ILS
NFAT TF pathway
MAP kinase activation in TLR cascade
Glutamate neurotransmitter release cycle
0
1
2
3
−log10 (adjusted p-value)

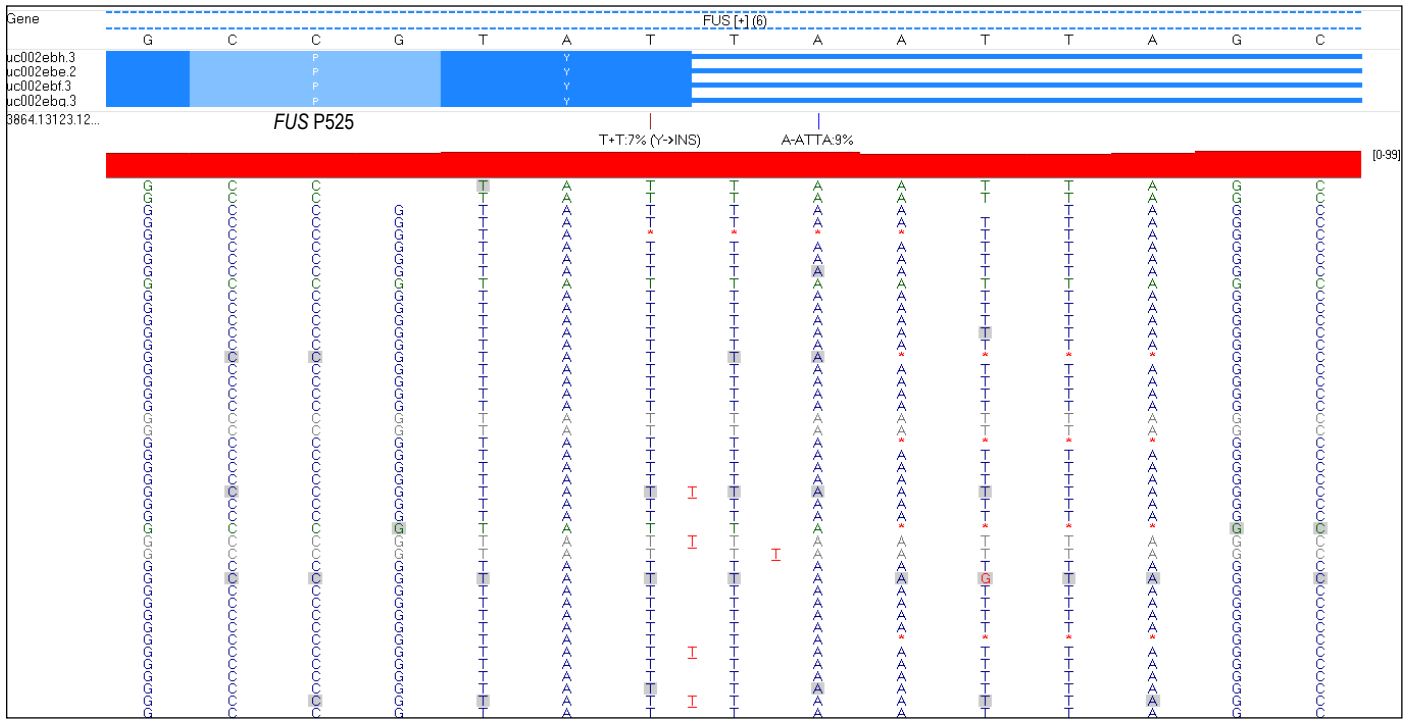
B
Gene
FUS [+] (6)
G C C G T A T T A A T T A G C
uc002ebh.3
uc002ebe.2
uc002ebf.3
uc002ebg.3
3864.13123.12...
FUS P525
T+T:7% (Y->INS)
A-ATTA:9%
[0-99]

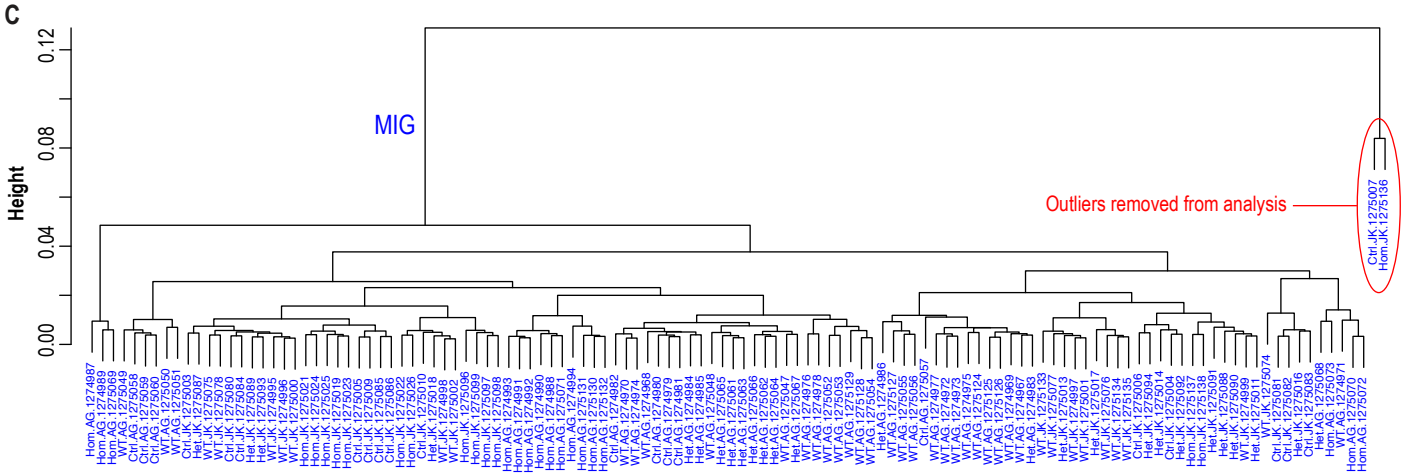
C
Height
0.00
0.04
0.08
0.12
MIG
Outliers removed from analysis
Ctrl.JK.1275097
Hom.JK.1275156

Figure S4. Homozygous *FUS* P525L MIGs display transcriptional perturbations of genes associated with characteristic microglial functions. Related to Figure 4.

(A) Top 20 MSigDB Canonical Pathways terms associated with genes enriched in the P525L Hom signature. Terms in blue are linked to characteristic features and functions of microglia. Red bars indicate that the majority of Hom signature genes associated with a term is upregulated; blue bars indicate the majority is downregulated. Multiple testing correction was performed using the Benjamini-Hochberg procedure to obtain adjusted *p*-values. See **Table S1** for more gene enrichment analysis results.

(B) Screenshot of RNA-seq reads aligned to the *FUS* locus for one of the JK WT MIG samples. A small percentage (11.9% ± 5.7%) of reads has a T insertion right after the last amino acid-coding codon which does not alter the FUS WT amino acid sequence but does extend the protein by 40 amino acids. Another small percentage of reads has an ATTA deletion within the stop codon (TAA) that simply reconstituted another stop codon (TAG) at the exact position. We deduced that our iPSC JK WT line was contaminated with cells harboring undesired CRISPR mutations and was hence not clonal.

(C) Hierarchical clustering of RNA-seq transcriptome profiles of MIGs differentiated from AG and JK lines with various *FUS* genotypes. The two outlier samples here are the same as two of those in the PCA plot (**Figure 4B**).

A

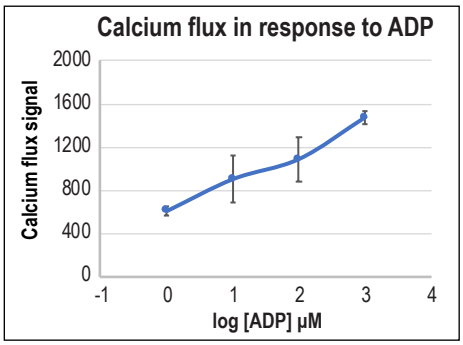
Calcium flux in response to ADP
Calcium flux signal
2000
1600
1200
800
400
0
-1
0
1
2
3
4
log [ADP] µM

B

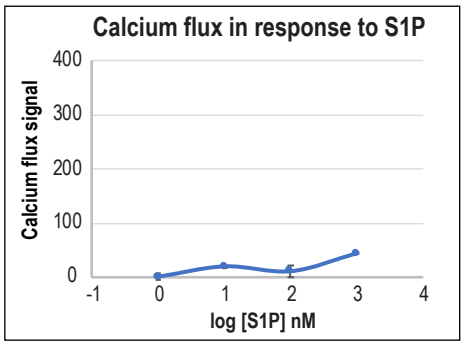
Calcium flux in response to S1P
Calcium flux signal
400
300
200
100
0
-1
0
1
2
3
4
log [S1P] nM

C

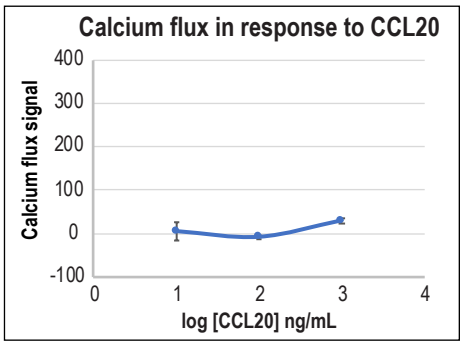
Calcium flux in response to CCL20
Calcium flux signal
400
300
200
100
0
-100
0
1
2
3
4
log [CCL20] ng/mL

D

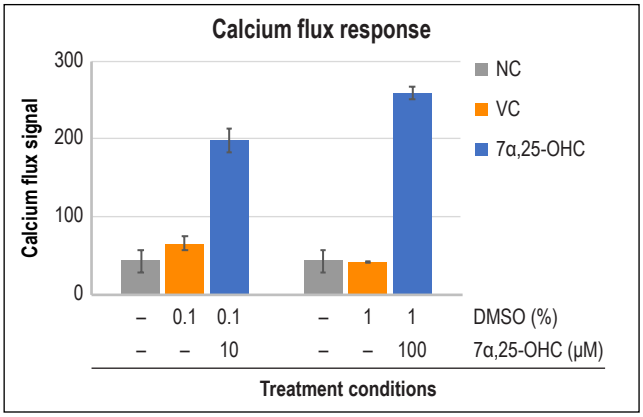
Calcium flux response
Calcium flux signal
300
200
100
0
NC
VC
7α,25-OHC
– 0.1 0.1 – 1 1
DMSO (%)
– – 10 – – 100
7α,25-OHC (µM)
Treatment conditions

Figure S5. Differentially expressed chemoreceptor genes in MIGs with *FUS* P525L mutations lead to perturbations of ligand-induced intracellular calcium signaling. Related to Figure 5.

(A, B, C) Intracellular calcium response to increasing concentrations of **(A)** ADP as positive control, **(B)** S1P, or **(C)** CCL20 in MIGs.

(D) Intracellular calcium response to 7α,25-OHC compared to the DMSO vehicle control (VC) and assay buffer-only negative control (NC) in MIGs.

Error bars represent standard deviation across two replicate wells in the JK line; $n = 2$. Datasets herein were not normalized to their Euclidean distance.

A

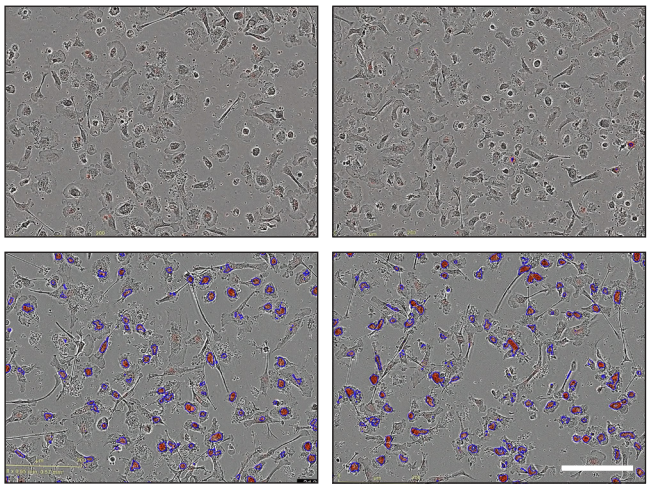

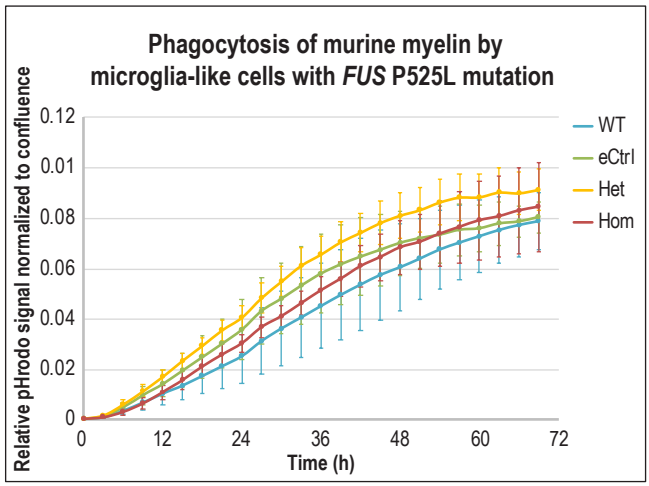

B

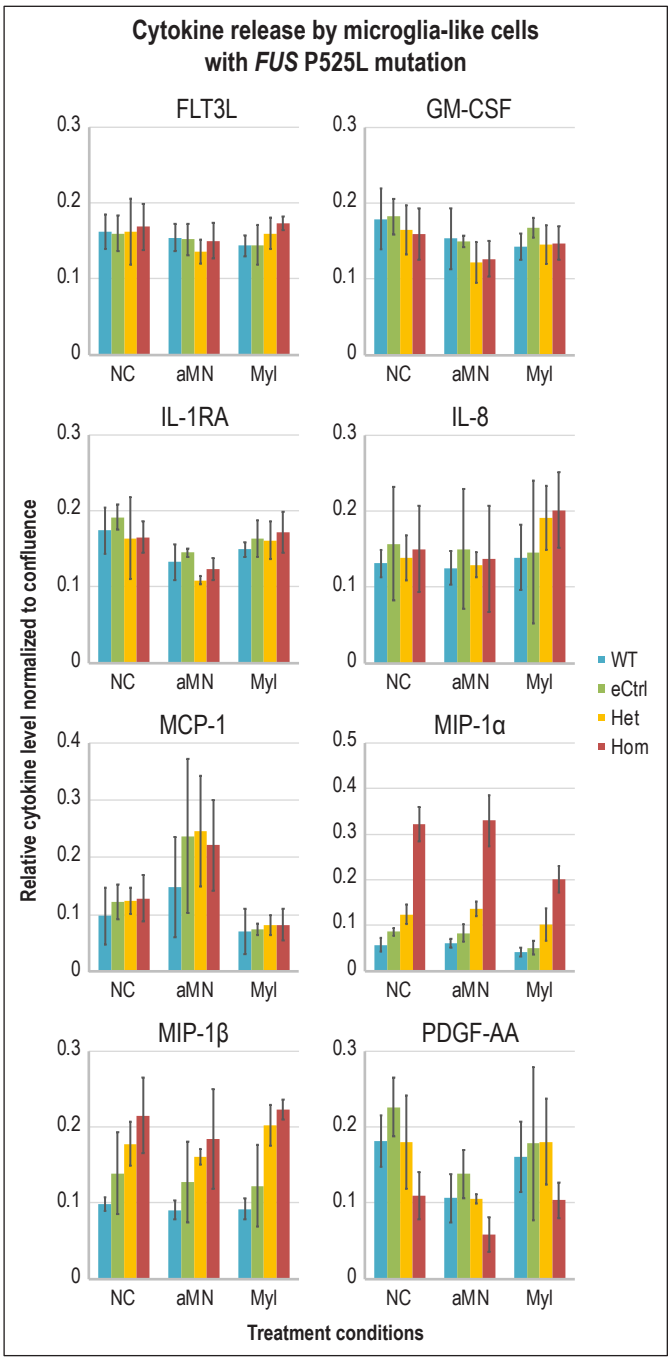

C

	G-CSF	GM-CSF	GRO-α	GRO-β	IL-1β
NC_6h	0.00	0.00	0.00	0.00	0.00
NC_24h	0.00	-1.16	0.00	0.00	0.00
NC_72h	0.00	2.18	0.00	0.00	0.05
aNeu_6h	0.11	-1.95	0.00	0.00	0.12
aNeu_24h	0.59	-1.96	0.00	0.00	0.00
aNeu_72h	0.36	1.72	0.00	0.00	0.00
Eco_6h	0.00	-0.62	0.00	0.00	1.90
Eco_24h	0.97	0.34	0.00	0.17	5.67
Eco_72h	5.42	3.38	2.32	3.99	6.02

	IL-1ra	IL-2	IL-6	IL-8	IL-10	IP-10	MCP-1	MIP-1α	MIP-1β	PDGF-AA	RANTES	TNF-α
NC_6h	0.00	0.00	0.00	0.00	0.00	0.00	0.00	0.00	0.00	0.00	0.00	0.00
NC_24h	1.11	0.00	-0.06	0.01	-0.37	0.00	0.00	0.00	0.00	0.00	-0.16	0.00
NC_72h	2.11	0.06	-0.09	2.94	-0.13	0.07	1.73	0.00	0.00	0.26	-0.16	0.00
aNeu_6h	0.40	0.00	0.00	-0.40	-0.23	0.00	0.00	0.00	0.00	0.06	-0.16	0.00
aNeu_24h	1.06	0.00	-0.09	0.14	-0.54	0.00	0.00	0.00	0.00	0.15	0.00	0.00
aNeu_72h	1.54	0.00	-0.04	3.21	-0.43	0.07	3.30	0.00	0.00	0.06	-0.10	0.00
Eco_6h	1.21	0.09	3.90	4.79	-0.13	0.00	0.00	3.14	0.61	0.18	0.05	5.22
Eco_24h	2.79	1.29	7.32	8.39	1.50	0.00	3.74	6.21	2.80	0.00	-0.05	6.81
Eco_72h	5.06	3.43	10.86	11.90	4.69	1.08	9.38	7.72	6.55	1.68	1.27	9.10

Figure S6. MIGs with *FUS* P525L mutations do not exhibit phagocytosis or cytokine release phenotypes. Related to Figure 6.

(A) Top half of panel: Phase contrast and red fluorescence overlay images of MIGs. Red fluorescence represents phagocytosed pHrodo-conjugated murine myelin while blue outline masks indicate signals above background. pHrodo is a pH-sensitive dye that is almost non-fluorescent at neutral pH but fluoresces brightly in acidic environments such as phagosomes. Due to space constraint, only representative images of WT and *FUS* P525L Hom cells are displayed. Scale bar = 200 μm. Bottom half of panel: Graph for phagocytosis signal normalized to cell confluence versus time from live imaging of MIGs with different *FUS* genotypes engulfing pHrodo-conjugated myelin. Error bars represent standard deviation across both AG and JK lines, each with at least three replicate wells; $n \geq 6$.

(B) Level of cytokine in cell culture supernatant released by MIGs under different treatment conditions after 72 h. NC: untreated negative control; aMN: apoptotic motor neurons; Myl: murine myelin. Presented here are cytokines that were above the detection limit of the immunoassay. Error bars represent standard deviation across both AG and JK lines, each with at least three replicate wells; $n \geq 6$.

(C) Cytokine level change in culture supernatant of MIGs under different treatment conditions after 6 h, 24 h, or 72 h. NC: untreated negative control; aNeu: apoptotic neurons; Eco: *E.coli*. Cytokine level in each condition was compared to that in NC at 6 h for the respective cytokine and reported as log2 fold-change (+/- mode). Only cytokines with log2 fold-change magnitude greater than 1 were shown. Presented here is the AG line with three replicate wells per condition.

Table S1: ***FUS*** **signature genes and their expression level fold-changes**

Table S2: **GO- and MSigDB Canonical Pathways-linked enriched genes in** ***FUS*** **P525L Hom signature.**

Table S3: **RT-qPCR of selected** ***FUS*** **P525L Hom signature genes**

Table S4: **Actively expressed microglia-enriched genes in primary human microglia and MIGs**

Movie S1. **Morphological and motile features of human iPSC-derived MIGs with homozygous FUS P525L mutations and isogenic control. Related to Figure 2.**

(A, B) Time-lapse movie of *FUS* (A) eCtrl and (B) P525L Hom MIGs. Phase contrast images were taken every 30 s over a period of 20 min; video speed increased 300 times. Presented here are clones from the AG line.

SUPPLEMENTAL EXPERIMENTAL PROCEDURES

Derivation of human iPSC lines

The human iPSC AG line was derived from male FibroGRO Xeno-Free Human Foreskin Fibroblasts (Sigma-Aldrich, Cat. #: SCC058) while the JK line was derived from male Neonatal Human Foreskin Fibroblasts (GlobalStem, Cat. #: GSC-3002). Both fibroblast lines were independently reprogrammed using the Simplicon RNA Reprogramming Kit (Sigma-Aldrich, Cat. #: SCR550) based on manufacturer's protocol. In brief, fibroblast cells were liposomally transfected with synthetic, self-replicating, non-integrating, polycistronic RNA transcripts encoding the reprogramming factors OCT-4, KLF-4, SOX-2, and GLIS1 as well as a puromycin resistance gene. B18R, encoded in co-transfected RNA transcripts and supplemented as proteins in cell culture media, was delivered to inhibit the cellular interferon response-mediated depletion of exogenous RNA. Transfected cells were then positively selected based on puromycin resistance before selectively degrading the transfected RNA by B18R withdrawal. Successful derivation of iPSCs were confirmed by checking for the expression of the pluripotency markers OCT-4, SOX2, NANOG, TRA-1-60, and TRA-1-81 via immunocytochemistry.

All iPSC lines were maintained on Geltrex Basement Membrane Matrix (Gibco, Cat. #: A1413301) in StemFlex medium (Gibco, Cat. #: A3349401) without antibiotics; incubated at 37ºC, 5% CO_2, and atmospheric O_2 level; and routinely passaged as cell clusters with ReLeSR (STEMCELL Technologies, Cat. #: 05872).

CRISPR engineering of iPSC lines

To genetically modify the *FUS* gene locus, CRISPR reagents were delivered into iPSCs by electroporation using the Neon Transfection System (Invitrogen, Cat. #: MPK5000S) according to manufacturer's protocol. Briefly, iPSCs were dissociated with TrypLE Select Enzyme (Gibco, Cat. #: 12563011) and $1x10^5$ cells were combined in 10 µL of Buffer R with 30 pmol of TrueCut Cas9 Protein v2 (Invitrogen, Cat. #: A36498), 30 pmol of each Alt-R CRISPR-Cas9 sgRNA (custom-made by Integrated DNA Technologies, Iowa, USA), and, when repair templates were required, 10 pmol of each ssODN (custom-made by Integrated DNA Technologies, Iowa, USA). The reaction mixture was then electroporated using the parameters 1300 V, 10 ms, and 3 pulses, before plating the cells on Geltrex matrix in StemFlex media supplemented with CloneR (STEMCELL Technologies, Cat. #: 05888) to increase single-cell survival. When recovered cells reached 75% confluence, they were dissociated into a single-cell suspension, seeded at a low density of 30 cells/cm^2, and cultured to form clonal colonies. Independent iPSC clones were then picked, screened for successful CRISPR modification using PCR and Sanger sequencing (service provided by Genewiz, New Jersey, USA), and checked to ensure no gross karyotypic and genomic abnormalities via aCGH and SNP microarray (services provided by Cell Line Genetics, Wisconsin, USA).

For generating the KO, two flanking sgRNAs with these target sequences were designed: Upstream, 5'-CTCCAGGCGTCGGTACTCAG-3'; Downstream, 5'-GAACTGGAATACAGTGTTCG-3'. For the other genotypes with point mutations, an sgRNA with this target sequence: 5'-GGGAGCCAGGCTAATTAATA-3', and the following ssODN repair templates were designed: P525L, 5'-TACTTAATTTTTTTTTTTTTTTTTGCAGGGGTGAGCACAGACAGGATCGCAGGGAGAGGCTGTATTAATTAGCCTGGCTCCCCAGGTTCTGGAACAGCTTTTTGTCCTGTACCCAGTGTTA-3'; eCtrl, 5'-TACTTAATTTTTTTTTTTTTTTTTTGCAGGGGTGAGCACAGACAGGATCGCAGGGAGAGGCCGTACTGATTAGCCTGGCTCCCCAGGTTCTGGAACAGCTTTTTGTCCTGTACCCAGTGTTA-3'.

Directed differentiation of human iPSCs into MIGs

Human iPSCs were directedly differentiated into MIGs based on the protocol from Douvaras *et al*. (2017)[1] with a few modifications. All differentiation factor proteins were procured from R&D Systems and all cell cultures were incubated at 37ºC, 5% CO_2, and atmospheric O_2 level. In brief, iPSC colonies were cut into square pieces using StemPro EZPassage Disposable Stem Cell Passaging Tool (Gibco, Cat. #: 23181010) and seeded at a density of 2.5 pieces/cm^2 on Matrigel Basement Membrane Matrix (Corning, Cat. #: 356231) in mTeSR1 medium (STEMCELL Technologies, Cat. #: 85850) containing 10 µM ROCK inhibitor Y-27632 (Tocris, Cat. #: 1254). The next day, medium was replaced with fresh mTeSR1. Three days post-seeding (Day 0), differentiation was initiated by applying 80 ng/ml BMP-4 (Cat. #: PRD314) in mTeSR1 for 4 days. On Day 4, medium was switched to StemPro-34 SFM (Gibco, Cat. #: 10639011)

containing 25 ng/ml bFGF (Cat. #: PRD233), 100 ng/ml SCF (Cat. #: PRD255), 80 ng/ml VEGF (Cat. #: PRD293), and 2 mM GlutaMAX Supplement (Gibco, Cat. #: 35050061) for 2 days. Henceforth, all media were supplemented with 2 mM GlutaMAX. On Day 6 and 10, media were replaced with StemPro-34 containing 50 ng/ml FLT3L (Cat. #: PRD308), 50 ng/ml IL-3 (Cat. #: PRD203), 50 ng/ml M-CSF (Cat. #: PRD216), 50 ng/ml SCF, and 5 ng/ml TPO (Cat. #: 288-TP) for 4 days respectively. From Day 14 onwards, every 3 to 4 days, media were replaced with StemPro-34 containing 50 ng/ml FLT3L (Cat. #: 308-FK-MTO), 25 ng/ml GM-CSF (Cat. #: 215-GM-MTO), and 50 ng/ml M-CSF (Cat. #: 216-MC-MTO).

Between Day 55 and 74, every 3 to 4 days, myeloid progenitor cells in the supernatant were harvested and plated at a density of $5x10^4$ cells/cm^2 on Laminin-521 (Gibco, Cat. #: A29248) in RPMI 1640 medium (Gibco, Cat. #: 11875093) supplemented with 10 ng/ml GM-CSF and 100 ng/ml IL-34 (Cat. #: 5265-IL-MTO) to be further differentiated into MIGs for 2 weeks. This microglia medium was also used for cell maintenance and refreshed every 3 to 4 days. MIGs were harvested using StemPro Accutase Cell Dissociation Reagent (Gibco, Cat. #: A1110501) and cryopreserved in CryoStor CS10 Freeze Media (BioLife Solutions, Cat. #: 210102) based on manufacturer's protocol. Cryopreserved MIGs were validated to be highly similar to their non-cryopreserved counterpart in terms of our *FUS* P525L Hom signature phenotype (**Table S3**).

Immunocytochemistry and confocal microscopy

Cells were cultured on 8-well chamber slides, fixed with 4% formaldehyde (Electron Microscopy Sciences, Cat. #: 15714-S) in PBS at room temperature (RT) for 15 min, and simultaneously permeabilized and blocked with 5% donkey serum (Jackson Immunoresearch, Cat. #: 017-000-121) and 0.2% Triton X-100 in PBS at RT for 1 hr. Primary antibody staining was performed at 4°C overnight and secondary antibody staining at RT for 1 hr, both in the permeabilization and blocking buffer. Three washes with PBS were performed after each antibody incubation step. Immunostained cells were subsequently mounted with Fluoromount-G Mounting Medium with DAPI (Invitrogen, Cat. #: 00-4959-52). Images were acquired under the Zeiss LSM 780 confocal microscope with the ZEN Black software and processed using the ImageJ software [2].

The following primary antibodies were used at the specified dilution: rabbit anti-FUS at 1:500 (Proteintech, Cat. #: 11570-1-AP; Abcam, Cat. #: ab84078), rabbit anti-MAP3K7 at 1:500 (Abcam, Cat. #: ab109526), mouse anti-MEF2C at 1:200 (Novus Biologicals, Cat. #: NBP2-00493), rabbit anti-TBK1 at 1:100 (Abcam, Cat. #: ab40676), and goat anti-TREM2 at 1:100 (R&D Systems, Cat. #: AF1828). The following donkey secondary antibodies from Invitrogen were used at 1:500 dilution: Alexa Fluor 488 anti-goat IgG (Cat. #: A11055), Alexa Fluor 555 anti-mouse IgG (Cat. #: A31570), Alexa Fluor 488 anti-rabbit IgG (Cat. #: A21206), and Alexa Fluor 555 anti-rabbit IgG (Cat. #: A31572).

Flow cytometry

Harvested cells were resuspended in PBS with LIVE/DEAD Fixable Near-IR Dead Cell Stain (Invitrogen, Cat. #: L10119) at 1:1000 dilution, incubated on ice for 15 min, washed with PBS, and centrifuged at 400 g for 2 min before aspirating supernatant. Pelleted cells were resuspended in PBS with 5% fetal bovine serum (FBS) (Gemini Bio, Cat. #: 100-500), Human BD Fc Block (BD Biosciences, Cat. #: 564219) at 1:20 dilution, and fluorophore-conjugated antibodies. Cells were incubated on ice for 20 min, washed using PBS with 5% FBS, and pelleted by centrifugation. Stained cells were then fixed by being resuspended in PBS with 2% formaldehyde and incubated at RT for 15 min, before being passed through the cap strainer of flow cytometry tubes (Corning, Cat. #: 352235). Whenever possible, cell samples and reagents were shielded from light and kept cold on ice. Flow cytometry was performed on the Beckman Coulter CytoFLEX LX machine using the CytExpert software and acquired data were analyzed using the FlowJo software.

The following fluorophore-conjugated antibodies were procured from BioLegend and used at 1:20 dilution unless otherwise stated: Alexa Fluor 488 anti-CD14 (Cat. #: 325610), Brilliant Violet 421 anti-CX3CR1 (Cat. #: 341620), Alexa Fluor 647 anti-MERTK (Cat. #: 367606), Brilliant Violet 605 anti-MRC1 (Cat. #: 321140), and PE anti-P2RY12 at 1:800 dilution (Cat. #: 392104).

RNA sequencing

Cells were homogenized in TRIzol (Invitrogen, Cat. #: 15596026) and chloroform was used for phase separation. The aqueous phase, containing total RNA, was purified using MagMAX-96 for Microarrays Total RNA Isolation Kit (Applied Biosystems, Cat. #: AM1839) and genomic DNA was

removed using RNase-free DNase Set (Qiagen, Cat. #: 79256). The mean RNA Quality Number (RQN) of all our samples was 9.43 ± 0.03. Strand-specific RNA-seq libraries were prepared from 500 ng of RNA using KAPA Stranded mRNA-Seq Kit (KAPA Biosystems, Cat. #: KK8401) and amplified by 12-cycle PCR. Sequencing was performed on the Illumina HiSeq 2000 Sequencing System by multiplexed paired-read run with 100 cycles. The resulting FASTQ files were analyzed via the FastQC software to ensure sufficient data quality. Subsequently, sequencing reads were mapped to the human genome (hg19) using the OmicSoft ArrayStudio software with two mismatches allowed. Across all our samples, the median of uniquely mapped paired reads was 86.09%.

All samples in the large dataset from which the differential gene expression analysis was performed were sequenced in the same batch to eliminate technical covariates. For quality control, the mean of the following parameters was obtained: Total Reads: $5.27 \times 10^7 \pm 7.90 \times 10^5$, Reads Mapped in Pair: 96.34% ± 0.10%, Reads Mapped to Gene: 90.60% ± 0.15%, Reads Mapped to Exon: 53.48% ± 0.14%, Reads Mapped to Exon Junction: 27.36% ± 0.09%, Reads Mapped to Intron: 9.76% ± 0.10%, Reads Mapped to rRNA: 3.61% ± 0.07%, Reads Mapped to Intergenic Region: 9.40% ± 0.15%.

Global similarity of samples based on RNAseq results was assessed via principal component analysis and hierarchical clustering. Based on the guidance described by Iglewicz and Hoaglin (1993)[3], z-score-based outlier detection was conducted for all sample sets shown in **Figure 3A**, **3B**, and **4B**. Each sample was projected onto the first two principal components. Next, the Euclidean distance between each sample and the mean of all samples (a.k.a. the centroid of all samples) was computed, and subsequently converted to a z-score by subtracting the mean distance and then dividing the difference by the standard deviation of the distances. Samples with an absolute z-score equal or greater than 3.5 were defined as outliers. The abnormality of the outlier samples was consistently supported by the observation that two outlier microglia samples wrongly clustered with progenitor samples in the pilot dataset (**Figure S3B**), and two outlier samples formed an isolated branch away from all other microglia samples in the hierarchical clustering of the large dataset (**Figure S4C**). The third outlier sample in the large dataset was flagged as an outlier due to its abnormal fibroblast-like morphology, prior to and independent of RNA-seq data analysis. These abnormal outliers were removed to ensure a high quality of the samples used in our analyses.

Reverse transcription-quantitative PCR

Messenger RNA from purified total RNA described above was reverse-transcribed into cDNA using SuperScript VILO Master Mix (Invitrogen, Cat. #: 11755500). The resulting cDNA was then amplified and quantified with the SensiFAST Probe Lo-ROX Kit (Meridian Bioscience, Cat. No: BIO-84050) using the QuantStudio 12K Flex Real-Time PCR System. An endogenous control gene (*ACTB*) was used to normalize any cDNA input differences. Data were reported via the comparative C_T (threshold cycle) method [4].

Intracellular calcium flux assay

Experimental parameters for the FLIPR Tetra High-throughput Cellular Screening System with ICCD Camera were set up as such: Exposure: 0.53 s, Camera Gain: 2000, Camera Gate: 6%, Addition Volume: 50 µL, Compound Concentration: 5-fold, Excitation LED: 470-495 nm, Emission Filter: 515-575 nm, LED Intensity: 30%, Addition Height: 225 µL, Tip Up Speed: 10 mm/s, Addition Speed: 10 µL/s. Using the Screenworks software, raw data were acquired as Relative Fluorescence Units (RFU) and processed by applying the kinetic reduction type of Max-Min across the entire acquisition period to obtain intracellular calcium flux signal values.

The following chemoreceptor ligands from Sigma-Aldrich were used: UDP (Cat. #: 94330), 7α,25-OHC (Cat. #: SML0541), S1P (Cat. #: 73914), CCL20 (Cat. #: SRP4491), and ADP (Cat. #: A2754); whereas the following chemoreceptor inhibitors were applied: MRS2578 (Cat. #: M0319) and NIBR189 (Cat. #: SML1981). In terms of solvents, 7α,25-OHC, MRS2578, and NIBR189 were dissolved in DMSO (Sigma-Aldrich, Cat. #: D2650); S1P in 0.3 M NaOH; and the other chemicals in ddH_2O. DMSO itself did not significantly elicit an intracellular calcium response in MIGs (**Figure S5D**).

Live-cell imaging for phagocytosis assays

MIGs were plated at 1×10^4 cells per well into flat-clear-bottom black-walled tissue culture-treated 96-well plates (Corning, Cat. #: 3904). At least 1 day later, assay dye reagent (as detailed below) was added. The plates were transferred into the Sartorius IncuCyte S3 Live-Cell Analysis System housed

within an incubator at 37ºC, 5% CO_2, and atmospheric O_2 level until the end of the assay. Nine tiled images per well from three replicate wells were taken every 3 hr for 72 hr using the 20X objective lens with phase contrast and red fluorescence acquisition at 400 ms of exposure. Data analysis was performed using the IncuCyte software to quantify the assay dye's red fluorescence signal in terms of integrated intensity as well as cell amount based on confluence for normalization.

Specific details for each following assay are further provided. (A) Apoptotic motor neuron efferocytosis assay: From the iCell Motor Neurons Kit (FUJIFILM Cellular Dynamics, Cat. #: 01279), $3.8x10^5$ human iPSC-derived motor neurons were seeded into a well of a clear tissue culture-treated 12-well plate and cultured for at least 1 week according to manufacturer's protocol. Motor neurons were then irradiated at 100 Jm^{-2} to induce apoptosis. Three days later, apoptotic motor neurons were dislodged by pipetting, harvested, and conjugated with pHrodo dye at a final concentration of 1 µg/mL using the IncuCyte pHrodo Red Cell Labeling Kit for Phagocytosis (Sartorius, Cat. #: 4649) based on manufacturer's protocol. In the last step, pHrodo-conjugated apoptotic motor neurons were resuspended in 5 mL of microglia medium and 100 uL per well of this suspension were used in the assay. (B) Myelin phagocytosis assay: Myelin was obtained from 3-month old C57BL/6 mouse brain as described in Larocca and Norton (2007) with minor modifications. In principle, brain tissue was homogenized in isotonic sucrose solution, followed by a cycling series of density gradient and differential centrifugation steps to isolate myelin membranes. Purified myelin was quantified based on protein content, adjusted to 1 mg/mL in PBS, triturated with an insulin syringe (BD, Cat. #: 328411), and labeled with 10 µg/mL pHrodo iFL Red STP Ester (Invitrogen, Cat. #: P36010) at RT for 45 min in the dark. Following centrifugation at 4000 g for 10 min, supernatant with unreacted dye was removed before resuspending myelin pellet in PBS. For the assay, approximately 1 ug per well of pHrodo-conjugated murine myelin was applied.

Cytokine profiling multiplex immunoassay

Cell culture supernatants from phagocytosis assays were gently collected without touching adherent cells at the desired time points. Released cytokines were then profiled using either the Human XL Cytokine Magnetic Luminex Performance Assay 45-plex Fixed Panel (R&D Systems, Cat. #: LKTM014) or the MILLIPLEX MAP Human Cytokine/Chemokine/Growth Factor Panel A 48 Plex Premixed Magnetic Bead Panel (Millipore, Cat. #: HCYTA-60K-PX48) according to manufacturer's protocol. In brief, supernatants from our experiments and cytokine concentration standards from the kit were incubated with a mixture of distinctly color-coded magnetic beads where each color encodes for specific capture antibodies against a particular cytokine target. Next, biotinylated detection antibodies against the capture antibodies were introduced before being reacted with fluorophore-conjugated streptavidin which serves as the reporter molecule. All washes to remove excess reagents were facilitated by immobilizing the beads with a handheld magnet. Identification and quantification of cytokines on the beads were then performed using the flow cytometry-based Luminex FLEXMAP 3D instrument with the xPONENT software. Acquired data were analyzed via the Millipore Belysa software to construct concentration standard curves from which absolute amounts of cytokine were inferred. We note that the assay performances of both commercial kits were very similar.

Statistical analysis for functional assays

For calcium assays, live-cell imaging, and cytokine profiling experiments, the dataset for each independent line in each experimental repeat (where applicable) was normalized by simple division with its Euclidean distance (square root of sum of squares of each data point). Within each *FUS* genotype, the normalized data points were then averaged across independent lines and experimental repeats (where applicable). Statistical analyses were performed using the unpaired *t*-test (one-tailed) on each of the other genotypes compared to WT. For RT-qPCR experiments, the paired *t*-test (one-tailed) was performed on P525L Hom compared to WT. Quantitative differences with $p < 0.05$ were considered significant.

SUPPLEMENTAL REFERENCES

1. Douvaras P, Sun B, Wang M, Kruglikov I, Lallos G, Zimmer M, *et al*. Directed Differentiation of Human Pluripotent Stem Cells to Microglia. Stem Cell Reports. 2017;8(6):1516-24.
2. Schneider CA, Rasband WS, Eliceiri KW. NIH Image to ImageJ: 25 years of image analysis. Nat Methods. 2012;9(7):671-5.
3. Iglewicz BH, D. C. How to detect and handle outliers. Milwaukee, Wisconsion: ASQC Quality Press; 1993.
4. Schmittgen TD, Livak KJ. Analyzing real-time PCR data by the comparative C(T) method. Nat Protoc. 2008;3(6):1101-8.
5. Larocca JN, Norton WT. Isolation of myelin. Curr Protoc Cell Biol. 2007;Chapter 3:Unit3 25.
6. Wagner GP, Kin K, Lynch VJ. A model based criterion for gene expression calls using RNA-seq data. Theory Biosci. 2013;132(3):159-64.